Journal of Aerosol Science 134 (2019) 34–55

Contents lists available at ScienceDirect

Journal of Aerosol Science

journal homepage: www.elsevier.com/locate/jaerosci

Lung aerosol dynamics of airborne influenza A virus-laden droplets and the resultant immune system responses: An in silico study

Ahmadreza Haghnegahdar, Jianan Zhao, Yu Feng*

School of Chemical Engineering, Oklahoma State University, Stillwater, OK, 74078, USA

ARTICLE INFO

Keywords:
Influenza A virus (IAV)-laden droplets
Computational fluid-particle dynamics (CFPD)
Host cell dynamics (HCD)
Adaptive immune system
Innate immune system

ABSTRACT

Influenza A Virus (IAV) replications start from the deposition of inhaled virus-laden droplets on the epithelial cells in the pulmonary tracts. In order to understand the local deposition patterns and within-host dynamics of infectious aerosols, accurate information of high-resolution imaging capabilities, as well as real-time flow cytometry analysis, are required for tracking infected cells, virus agents, and immune system responses. However, clinical and animal studies are in deficit to meet the above-mentioned demands, due to their limited operational flexibility and imaging resolution. Therefore, this study developed an experimentally validated multiscale numerical model, i.e., the Computational Fluid-Particle Dynamics (CFPD) plus Host Cell Dynamics (HCD) model, to predict the transport and deposition of the low-strain IAV-laden droplets, as well as the resultant regional immune system responses. The hygroscopic growth and shrinkage of IAV-laden droplets were also accurately modeled. The subject-specific respiratory system was discretized using polyhedron-core meshes. By recreating both mouth and nasal breathing scenarios, simulations of isotonic IAV-laden droplets with three different compositions were achieved. It is the first time that parametric analysis has been performed to investigate how different exposure conditions can influence the IAV aerodynamics in the lung and the subsequent immune system responses. Numerical results show a higher viral accretion followed by a faster immune system response in the supraglottic region when IAV-laden droplets with the higher NaCl concentration were inhaled. Consequently, more severe symptoms and longer recovery are expected at the pharynx. Furthermore, local deposition patterns of IAV-laden droplets and post-deposition infection dynamics provide direct quantitative evidence to enhance the fundamental understanding of the underlying mechanisms for upper airway and lower airway infections.

1. Introduction

Influenza A virus (IAV) is highly transmissible as one of the leading causes of pulmonary infections (Boianelli et al., 2015). Three circulating subtypes, i.e., type A H1N1, type A H3N2, and type B, can infect humans and result in massive global epidemics. IAVs pass among individuals through the airborne sneeze or cough droplets released by the infected. Such airborne transmissions of infectious substances expelled from the respiration system of an infected patient is commonly known to be the key contagion mechanism (Eames, Tang, Li, & Wilson, 2009). Subsequently, the influenza virus replicates in epithelial cells throughout the lung airways, with the virus being recoverable from both the upper and lower respiratory tracts that are naturally or experimentally infected. Epithelial cells in the tracheobronchial tree are the primary sites of IAV replication. The pulmonary deposition of virus-laden droplets imposes

* Corresponding author.
E-mail address: yu.feng@okstate.edu (Y. Feng).

https://doi.org/10.1016/j.jaerosci.2019.04.009
Received 14 November 2018; Received in revised form 14 March 2019; Accepted 10 April 2019
Available online 25 April 2019

warning signals to the immune system, which is a complex and nonlinear interaction of the host cells and antigen structure. Lower airway infections can result in the flooding of alveolar sacs, developing acute respiratory distress syndrome, and causing fatalities because of respiratory failures. Airborne transmission of the IAV-laden droplets occurs when the viral load migrates through nasal and mouth breathing or paranasal sinuses (ocular route) to the airways. The airborne transmission of infectious substances expelled by an infected subject is commonly known to be the decisive contagion mechanism. Meanwhile, the underlying principles of how IAVs cause different pathogenic profiles has not been well studied. Investigating local deposition patterns and within-host dynamics require high-resolution imaging capabilities as well as real-time flow cytometry analysis of the infected cells, virus agents, and immune system responses. However, clinical and animal studies are in deficit to meet such demands. To address the deficiency, this study developed a new multiscale model by integrating the computational fluid-particle dynamics (CFPD) model and the host cell dynamics (HCD) model, to simulate the transport and deposition of IAV-laden droplets and predict the regional immune system responses of infected host cells. Deposition patterns of IAV-laden droplets and post-deposition infection dynamics provide informative data, which will significantly enhance the fundamental understanding of how exposure to the airborne IAV-laden aerosols can lead to the lower airway infection.

Research efforts and general findings from early studies are summarized as follows. To the best of our knowledge, there is no existing multiscale model which is capable of simulating the transport and deposition of virus-laden droplets, as well as the resultant immune system responses simultaneously. However, many numerical studies have been done separately focusing on modeling either the droplet transport dynamics in the lung or the viral dynamics in host cells. Lambert, O'shaughnessy, Tawhai, Hoffman, and Lin (2011) performed multiphase flow simulations of the transport of pure water droplets with a constant diameter of 2.5 μm. Exposure through mouth breathing showed a higher deposition in the upper airway and the first bifurcation. Using the CFPD model, another numerical study (Kreidenweis et al., 2005; Mikhailov, Vlasenko, Niessner, & Pöschl, 2004) determined that particles greater than 6 μm deposited in the upper respiratory tract. Those particles between 2 to 6 μm mostly deposited in the 2nd generation (G2), and smaller particles would reach lower lobes (Darquenne, 2012; Ou, Li, Wei, Yen, & Deng, 2017). As a key mechanism for IAV-laden droplet aerodynamics, the hygroscopic growth and shrinkage of particulate matters in humid air were initially modeled and investigated in climate science. In lung aerosol dynamics research, inhalable droplet size change dynamics were studied in idealized upper airway geometries (Feng, Kleinstreuer, Castro, & Rostami, 2016; Zhang, Kim, & Kleinstreuer, 2006), in the subject-specific human upper airway geometry excluding the nasal cavity (Worth Longest & Xi, 2008), and in the nasal cavity (Schroeter et al., 2016). Existing studies mentioned above show that the evaporation and condensation of droplets were dependent on the droplets composition, the ambient relative humidity (RH), temperature, and pressure. Droplet trajectory also depends on the ambient airflow patterns. Specifically, breathing through mouth or nose can change the local airflow velocity distributions and consequently the droplet heat and mass transfer.

Once the droplets deposit on the mucus layer, IAVs will bind to the surface of targeted epithelial cells. The endocytosis of the virions inside the epithelial cell occurs after 20 minutes post-infection (Oguin et al., 2014). At this stage, the virus binds to the epithelial cell for cloning and reproducing copies of RNA and viral proteins, which is also known as the incubation period. Eclipse phase (Pinilla, Holder, Abed, Boivin, & Beauchemin, 2012) is the period between post-infection and reproducing stage. The duration of this phase is predicted from 5 to 12 hours post-infection (Beauchemin & Handel, 2011) and can reach the peak value after 2–3 days post-infection (dpi) (Boianelli et al., 2015). Accordingly, the innate and adaptive immune systems (IIS and AIS respectively) will be activated and interfere with the antigen replication. Mathematical models for the viral dynamics within the host, i.e., host cell dynamics (HCD) models, were developed separately in existing studies with various considerations for the interactions between the targeted cell, immune system, and viral agents (Beauchemin & Handel, 2011; Smith & Perelson, 2011). The first attempt to numerically represent the HCD was done by Larson, Dominik, Rowberg, and Higbee (1976) after fitting the data from IAV H3N2 infected Swiss-ICR mice. The viral doses in the lung, trachea, and nasopharynx were investigated with five associated rate parameters. Formulating the HCD using target cell models, Nowak and May (2000) paved a new roadmap on the IV infection study. Baccam, Beauchemin, Macken, Hayden, and Perelson (2006) adopted target cell models by including susceptible cell, infected cell, and virus to fit a model with the *in vivo* data of the virus A/Hong Kong/123/77 (H1N1) infected human. Specifically, the eclipse phase was included by considering a latent phase for the infected cell before becoming productive. Their numerical results suggest that the virus reproduction started at 6 hours post-infection and the infected cells lifetime was 11 h. Holder and Beauchemin (2011) investigated the same mathematical model for validation of *in vitro* study and suggested a more complex parameter for the infected cells in the delayed phase. Petrie et al. (2013) developed a double target cell model for human infections with avian strain by differentiating target cells into two fractions, i.e., default and secondary cells. The response from the immune system by proposing the effect of Abs and $CD8^+$ T cells was first introduced into the model by Bocharov and Romanyukha (1994). Baccam et al. (2006) considered the (IFN)-I dynamics and their results show double peaks in viral titer data. Moreover, the additional factor of NK cells was introduced to the target cell models by Canini and Carrat (2011), where the NK activation is triggered by (IFN)-I. Specifically, the virus kinetics and symptom dynamics population have been utilized to estimate infection parameters. Attempts on including the AIS with $CD8^+$ T cells and Abs into the cell population models were projected by Lee et al. (2009). Specifically, a lymphatic compartment was considered to represent the activation of T and B cells. In this regard, 10 equations for the kinetics of AIS components at different stages were added to the target model and the optimum time of antiviral drug administration was proposed to be at 2 dpi. For model optimization and validation, existing *in vitro* and *in vivo* studies have categorized the key mechanisms in the HCD model (Baccam et al., 2006; De Andrea, Ravera, Gioia, Gariglio, & Landolfo, 2002; Male, Brostoff, Roth, & Roitt, 2006; Miller & Mitchell, 1969). Specifically, immune subsystem responses and processes are in a collocative multi-directional state compared to each other, that any changes in a factor would influence intensively on the enhancement or suppression of the others. The immune response processed by lymphoid tissues and leukocytes in a process that can be explained by recalling two lines of defense: (1) Innate immune system

response (IISR): released interferons (IFN)-I from the invaded cells and Natural Killers (NK) cells; and (2) adaptive immune system response (AISR): humoral response (antibody mediated) and cytotoxic lymphocytes agents (Cytotoxic and Helper T cells, B cells) with the activation dependency on dendritic cell and IAV population.

Since the infection and replication are significantly dependent on the population of the above-mentioned agents, it is necessary to combine the CFPD model and the HCD model in order to be capable of provide accurate and noninvasive predictions. Indeed, the CFPD model is able to address the deficiency of the HCD model by providing precise estimations of the regional IAV deposition data in human respiratory systems under realistic exposure conditions, which are not achievable by any existing numerical models. Therefore, an experimentally validated multiscale model, i.e., a CFPD-HCD model, was developed and employed in this study to simulate the transport of the respired IAV-laden droplets, and predict the immune system response at a time span of 12 days post-infection (dpi). To the best of our knowledge, this is the first time that virus-laden droplet transport, size change dynamics, deposition, and replication, as well as the resultant immune system responses, have been systematically studied in a subject-specific human respiratory system under various exposure conditions using a validated noninvasive multiscale numerical model.

2. Methodology

An experimentally validated multiscale model, i.e., the CFPD-HCD model was developed and employed to simulate the transport of inhaled IAV-laden droplets and the resultant immune system response at a time span of 12 dpi. The CFPD-HCD model consists of two simulation layers, which are connected at the airway mucosa lining based on the fact that the viral replications start from the deposition of inhaled fomites on the epithelial cells. Since the infection replication is significantly dependent on the local host cell population and immune system agents, the CFPD model with the Euler-Lagrange scheme was adopted to simulate the virus-laden droplets aerodynamics in the lung. Using such a modeling scheme, the CFPD model can provide more realistic local and regional lung uptake predictions than the existing numerical studies only with the HCD model. Localized deposition patterns were simulated and transferred as the inputs to the HCD model to determine the regional host dynamic responses.

Fig. 1 shows the schematic of the workflow for the CFPD-HCD model. Instead of tetrahedron-core meshes used in early studies (Feng et al., 2016, 2018; Zhang et al., 2006), the polyhedron-core mesh was generated considering the better computational efficiency and stability. The final mesh has 18,453,311 elements including near-wall prism layers (see the SI for the details of mesh independence test). The inhaled number concentration of IAV-laden droplets after the exposure to sneezing events by the infected subject was estimated based on a separation distance of 3 feet (Hamborsky et al., 2015; Liu, Li, Nielsen, Wei, & Jensen, 2017). The indoor condition with artificial heating at the winter time is set up for the inhalation condition (Knight, 1980). The unimodal droplet size distribution was defined using 6 size bins based on the statistics reported by Duguid (1946). Two breathing patterns, i.e., mouth and nasal breathings, were simulated using realistic human breathing waveforms of complete inhalation-exhalation cycles. Moreover, the condensation and evaporation between droplets and the surrounding humid air were modeled by solving the energy and mass balance equations for each droplet. Since the hygroscopic growth behavior of droplets is highly dependent on their contents (Feng et al., 2016; Zhang et al., 2006), three compositions were selected for the parametric analysis on how droplet ingredients can influence the droplet size change dynamics and the resultant transport and deposition in human respiratory systems and the immune system responses. Based on the fact that NaCl and water are the two major components of the coughing or sneezing droplets (Effros et al., 2002), NaCl-water binary mixtures are assumed for the droplet composition. The investigated cases with different breathing patterns and droplet compositions in mass fractions are listed as follows:

- Realistic nasal breathing (NB) exposed to a sneezing event:
  - Case 1: 100.0% water - 0.0% NaCl,
  - Case 2: 93.2% water - 6.8% NaCl (Schaffer, Soergel, & Straube, 1976),

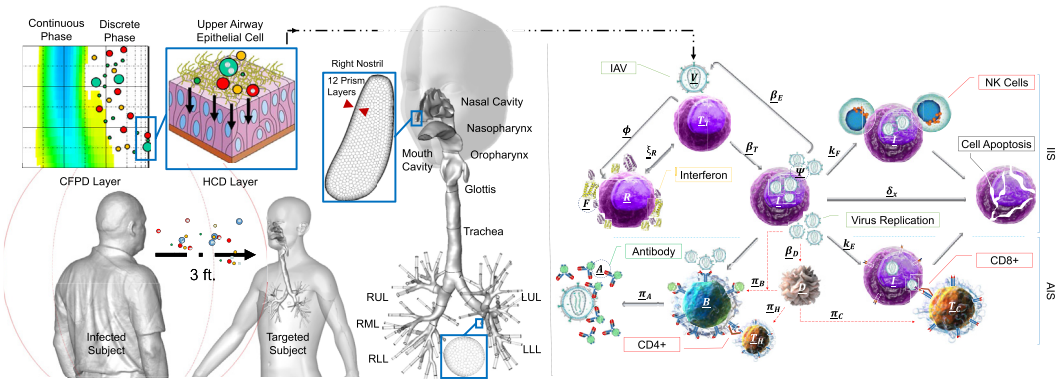

Fig. 1. The framework of the multiscale CFPD-HCD model for the human-to-human IAV infection with a subject-specific airway geometry. The description of the HCD model is given in Section 3.2. The detail of the final polyhedral-core mesh is provided at the right nostril and an airway outlet (RUL: right upper lobe, RML: right middle lobe, RLL: right lower lobe, LUL: left upper lobe, LLL: left lower lobe).

- Case 3: 89.6% water - 10.4% NaCl (Yang & Marr, 2011),
- Realistic mouth breathing (MB) exposed to a sneezing event:
  - Case 4: 100.0% water - 0.0% NaCl,
  - Case 5: 93.2% water - 6.8% NaCl,
  - Case 6: 89.6% water - 10.4% NaCl.

3. Governing equations

3.1. Computational fluid-particle dynamics (CFPD)

The transport of IAV-laden droplets in the subject-specific human respiratory system starts from inhaling airborne IAV aerosols sneezed or coughed out of an infected subject. Due to the low volume fraction of IAV-laden droplets in the air, the one-way coupled Euler-Lagrange scheme was adopted in this study (Feng et al., 2018). The liquid-vapor interaction was considered by predicting the droplet size change dynamics during their transport in the respiratory system. These effects were modeled by solving supplementary equations, i.e., heat and mass balance equations for droplet and vapor phases. Details are provided as follows:

3.1.1. Eulerian phase: the air-water vapor mixture

Based on the fact that the laminar-to-turbulence transitional flow regime exists at the nasopharynx and the epiglottis in the subject-specific human respiratory system employed in this study (Feng et al., 2018), turbulence models that can capture the transitional sites need to be employed. Indeed, precise predictions of the airflow field are important to determine deposition patterns in lung airways (Ma & Lutchen, 2009). In this study, The Transition Shear Stress Transport (SST) model (Feng et al., 2018; Menter, 1994) is employed that takes the ability of the $k-\omega$ model in representing the near-wall boundary layers and is combined with the $k-\varepsilon$ model to solve the free-stream airflow (Langtry & Menter, 2009). The SST model accompanied with the momentum equation are presented as follows:

$$\rho\left(\frac{\partial u_i}{\partial t}+u_j\frac{\partial u_i}{\partial x_j}\right)=-\frac{\partial p}{\partial x_i}+\frac{\partial}{\partial x_j}\left[(\mu+\mu_t)\left(\frac{\partial u_i}{\partial x_j}+\frac{\partial u_j}{\partial x_i}\right)\right]+\rho g_i \tag{1}$$

$$\frac{\partial}{\partial t}(\rho\kappa)+\frac{\partial}{\partial x_i}(\rho u_i\kappa)=\frac{\partial}{\partial x_i}\left[(\mu+\mu_t\sigma_\kappa)\frac{\partial\kappa}{\partial x_i}\right]+\widetilde{G}_\kappa-Y_\kappa \tag{2}$$

$$\frac{\partial}{\partial t}(\rho\omega)+\frac{\partial}{\partial x_i}(\rho u_i\omega)=\frac{\partial}{\partial x_i}\left[(\mu+\mu_t\sigma_\omega)\frac{\partial\omega}{\partial x_i}\right]+G_\omega-Y_\omega+Cd_\omega \tag{3}$$

$$\frac{\partial}{\partial t}(\rho\gamma)+\frac{\partial}{\partial x_i}(\rho u_i\gamma)=\frac{\partial}{\partial x_i}\left[\left(\mu+\frac{\mu_t}{\sigma_f}\right)\frac{\partial\gamma}{\partial x_i}\right]+G_\gamma-Y_\gamma \tag{4}$$

$$\frac{\partial}{\partial t}(\rho\widetilde{Re}_{\theta t})+\frac{\partial}{\partial x_i}(\rho u_i\widetilde{Re}_{\theta t})=\frac{\partial}{\partial x_i}\left[\sigma_{\theta t}(\mu+\mu_t)\frac{\partial\widetilde{Re}_{\theta t}}{\partial x_i}\right]+G_{\theta t} \tag{5}$$

where ρ is the density of the air-water vapor mixture, u_i is the mixture stream velocity vector, and μ is the gas mixture molecular dynamic viscosity. In addition, μ_t is the turbulent viscosity given as $\mu_t=\rho c_\mu f_\mu k/\omega$ and f_μ is a function of $R_T=\rho k/(\mu\omega)$ and other turbulence constants reported by Wilcox et al. (1998). In Eqs. (2)–(5), G and Y account for the production and dissipation of the turbulence kinetic energy (k) and the rate of dissipation of k into internal thermal energy (ω) due to turbulence. Also, σ_k and σ_ω are turbulent Prandtl numbers, which are equal to 0.85 and 0.75 respectively. The calculation of intermittency generation in Eq. (4) (G_γ) is performed by the transported Reynolds number ($\widetilde{Re}_{\theta t}$) in Eq. (5).

Furthermore, governing equations for the mass conservation of the air-water vapor mixture are:

$$\frac{\partial(\rho Y_s)}{\partial t}+\frac{\partial(\rho u_i Y_s)}{\partial x_j}=-\frac{\partial J_s}{\partial x_j}+S_s^m \tag{6}$$

in which Y_s is the vapor species mass fraction. The mixture is a combination of air, water vapor, and a negligible amount of NaCl in vapor form. J_s is the mass diffusion flux of species due to concentration gradient. To calculate J_s, the Fick's Law can be employed and given as:

$$J_s=-\left(\rho D_s^m+\frac{\mu_t}{Sc_t}\right)\frac{\partial Y_s}{\partial x_j} \tag{7}$$

where D_s^m is the molecular diffusivity of the species in the Euler phase. Sc_t is the turbulent Schmidt number, i.e., $Sc_t=\mu_t/(\rho D_t)$ and D_t is the turbulent diffusivity. In this study, Sc_t is assumed to be 0.9 (Zhang, Kleinstreuer, & Feng, 2012a). In Eq. (6) , S_i^m $[kg/(m^3s)]$ is the mass source term, i.e., the rate of species mass transfer between liquid and vapor phases.

The conservation of energy for the air-water vapor mixture can be given as:

$$\frac{\partial(\rho c_p T)}{\partial t} + \frac{\partial(\rho u_i c_p T)}{\partial x_j} = \frac{\partial}{\partial x_j}\left[(k_c + k_{c,t})\frac{\partial T}{\partial x_j} - \sum_s h_s J_s\right] + \Phi_{vd} + S^T \tag{8}$$

where c_p, T, Φ_{vd}, k_c, and $k_{c,t}$ are the gas mixture specific heat, cell center temperature, viscous dissipation, gas mixture turbulent conductivity, and turbulent thermal conductivity, respectively. Moreover, $k_{c,t} = c_p\mu_t/Pr_t$, in which the turbulent Prandtl number $Pr_t = c_p\mu/k_c$. h_s is the sensible enthalpy of the species calculated by considering 298.15 K as the reference temperature.

With the unsteady particle tracking in a local control volume (ΔV), two different time steps are defined. Δt_f is the flow time step and Δt_d is the discrete droplet time step. Transient simulations of the inter-phase source terms using implicit solver is performed by advancing the DP at the beginning of a new flow time step calculation. Specifically, the mass source term can be defined as:

$$S_s^m = \sum_{parcels}\left((\dot{m}_d^0/m_d^0)N_{d/parcel}\int_{t_f^0}^{t_f^0+\Delta t_d}\frac{dm_d}{dt_d}\,dt_d\right)/\Delta V \tag{9}$$

where $N_{d/parcel}$ is the number of droplets in each "parcel", i.e., a combination of droplets with the same diameter existing in the same volume control.

The energy source term S^T $[W/m^3]$ was calculated by considering the latent heat of evaporation/condensation between phases:

$$S^T = \sum_{parcels}\left[(\dot{m}_d^0/m_d^0)N_{d/parcel}\left(H_{lat}\int_{t_f^0}^{t_f^0+\Delta t_d} dm_d + \Delta E\right)\right]/\Delta V \tag{10}$$

$$\Delta E = (m_d c_p T_d)|_{t_f^0} - (m_d c_p T_d)|_{t_f^0+\Delta t_d} \tag{11}$$

where H_{lat} is the latent heat of energy exchange between the phases. The subscripts of t_f^0 and $t_f^0 + \Delta t_d$ show the flow times before and after the current loop. In addition, to distribute the effect of the parcel's mass and energy source terms to neighboring mesh nodes, the nodes-per-cell averaging was performed for the continuous phase by dividing S_s^m and S^T by the number of mesh nodes at each control volume. The advanced averaging technique results in better stability in the calculation of mass and energy equations.

3.1.2. Lagrangian phase: IAV-laden droplets transport and size change dynamics

With the dilute suspension assumption and the negligible droplet rotational motion, the unsteady DP tracking is performed by calculating a series of equations, i.e., the translational equation, as well as the mass and energy conservation equations for each droplet.

$$\frac{d}{dt_d}(m_d u_{d,i}) = F_{d,i}^D + F_{d,i}^L + F_{d,i}^{BM} + F_{d,i}^G \tag{12}$$

The superscripts of D, L, BM, and G represent drag force, Saffman lift force, Brownian motion force, and gravity, respectively. The details of each force acting on the spherical droplet can be found in Feng et al. (2018).

Forces acting on the droplets can be accurately predicted by recovering the local turbulence fluctuation velocity components (Feng & Kleinstreuer, 2013). In detail, the eddy lifetime model is employed, which assumes the interaction of particles with turbulence eddies is identified by the Gaussian probability distribution of fluctuation velocity ($u'_i = G_{u'}\sqrt{\overline{u'_i}^2}$) and the lifetime of the turbulence eddies can be given as (Daly & Harlow, 1970):

$$\tau_{E-L} = C_\mu\frac{\kappa}{0.09\kappa\omega} \approx \frac{0.30}{0.09\omega} \tag{13}$$

However, the default eddy lifetime model can overestimate the near-wall fluctuation velocity by neglecting the anisotropic fluctuation velocity components in different directions (Feng & Kleinstreuer, 2013). Thus, the near-wall correction is employed by introducing a damping function (Wang, James, & et al, 1999; Feng & Kleinstreuer, 2013).

$$\frac{dm_d}{dt_d} = \rho K_{mc} A_d \ln\left(\frac{1 - Y_{s,\infty}}{1 - Y_{s,S}}\right) \tag{14}$$

where $Y_{s,S}$ and $Y_{s,\infty}$ are the mass fraction of species s at the droplet surface and at the surrounding continuous phase, i.e., the center of the cell where the droplet is residing. A_d is the droplet surface and K_{mc} is the mass transfer coefficient [m/s] given as:

$$K_{mc} = \left[\frac{1 + Kn}{1 + \left(\frac{4}{3\alpha_m} + 0.377\right)Kn + \frac{4}{3\alpha_m}Kn^2}\right]\frac{D_s^m}{d_d^V}Sh \tag{15}$$

In Eq. (15), the first parameter shows the non-continuum effect for the submicron droplets, where $\alpha_m = 1$ is the mass accommodation coefficient (Hinds, 2012) and the Knudsen number is defined as $Kn = 2\lambda/d_d^V$, in which λ is the mean free path of the continuous phase gas mixture and d_d^V is the droplet diameter. In addition, the Sherwood number (Sh) can be calculated by Whitaker (1972):

$$Sh = 2.0 + (0.4Re_d^{1/2} + 0.006Re_d^{2/3})Sc^{0.4}(\mu/\mu_{d,S})^{1/4} \tag{16}$$

where Re_d is the droplet Reynolds number. Also, μ and $\mu_{d,S}$ are the gas mixture viscosities at the droplet ambient temperature and droplet surface temperature, respectively.

The threshold between the evaporation and condensation processes is defined by the thermodynamic properties of the droplet, i.e., equilibrium partial vapor pressures, the temperature at the dew point, and mass fraction of droplet components. For evaporation, any droplet that shrinks under $d_d^V = 0.01$ nm, i.e., 0.05% of the IAV minimum diameter, is considered to be completely evaporated.

The partial vapor pressure at the droplet surface can be significantly influenced by two effects: (1) the Kelvin effect, and (2) the solute effects. Based on the cloud physics for the multicomponent droplet with an ionic solute, the Köhler theory is employed to update the droplet compositions (Kreidenweis et al., 2005; Mikhailov et al., 2004). Specifically, the mass fraction can be calculated by:

$$Y_{s,S} = \frac{P_{s,S}}{P^0(T)} = \gamma_s \exp\left(\frac{4\sigma_d \overline{V_s}}{RT_d d_d^V}\right) \tag{17}$$

where $P_{s,S}$ and $P^0(T)$ are the vapor pressure at the droplet surface and the saturation vapor pressure of the transferred species at the temperature of the control volume where the droplet is located. σ_d is the surface tension of the droplet solution, R is the universal gas constant, γ_s is the species activity coefficient, and $\overline{V_s}$ is the partial molar volume of solute NaCl. It can be estimated by the following equations:

$$\overline{V_s} = \frac{MW_s}{\rho_{sol}}\left(1 + \frac{Y_{d,NaCl}}{\rho_{sol}}\frac{d\rho_{sol}}{dY_{d,NaCl}}\right) \tag{18}$$

$$\gamma_s = \exp(\vartheta_{d,s}\Phi_{d,s}MW_{d,water}\tilde{m}_{d,NaCl}) \tag{19}$$

In Eqs. (18) and (19), MW_s represents the species molecular weight, ρ_{sol} is the droplet solution density, $\vartheta_{d,s}$ is the stoichiometric dissociation number of the solute ($\vartheta_{d,s} = 2$ for NaCl), and $\Phi_{d,s}$ is the molal osmotic coefficient of the solute in the solution. Also, $\tilde{m}_{d,NaCl} = Y_{d,NaCl}/[MW_{d,NaCl}(1 - Y_{d,NaCl})]$ is the molality (m) of the solution. The solute effect is represented in the formulation of activity coefficient and the Kelvin effect is showed in Eq. (17). It is worth mentioning that for a dilute solution, Eqs. (18) and (19) can be simplified as:

$$\overline{V_s} = \frac{MW_s}{\rho_{sol}} \tag{20}$$

$$\gamma_{water} = \left(1 - \varrho\frac{Y_{d,NaCl}\,MW_{d,water}}{x_{d,water}\,MW_{d,NaCl}}\right)/x_{d,water} \tag{21}$$

where ϱ is the Van't Hoff factor. $x_{d,water}$ is the mole fraction of water and can be calculated by:

$$x_{d,water} = \frac{Y_{d,water}\,MW_{d,water}}{\sum_{d,s} Y_{d,s}\,MW_{d,s}} \tag{22}$$

In Eqs. (17)–(20), parameters are extensively dependent on the temperature and composition of the droplet. Correlations and experimental data that were utilized to calculate these parameters are listed in Table 4. The energy balance equation for each droplet can be given as:

$$\frac{dT_d}{dt_d} = \left[K_{hc}A_d(T - T_d) - \frac{dm_d}{dt_d}H_{lat}\right]/m_d c_{p,d} \tag{23}$$

where K_{hc} is the heat transfer coefficient. Lewis number is assumed to be equal to 1, and a negligible influence of the evaporated/condensed species in the DP on the gas mixture specific heat results in:

$$K_{hc} = K_{mc}\frac{Nu\,k_c}{Sh\,D_s^m} \tag{24}$$

In Eq. (24), Nu is the Nusselt number and can be given as:

$$Nu = 2.0 + (0.4Re_d^{1/2} + 0.006Re_d^{2/3})Pr^{0.4}(\mu/\mu_{d,S})^{1/4} \tag{25}$$

Eq. (23) is based on the assumption that the droplet is at a uniform temperature and the DP has a negligible internal resistance to the heat transfer. Also, the derivation and validation of Eqs. (14) and (23) are provided by Miller, Harstad, and Bellan (1998).

3.2. The host cell dynamics (HCD) model

Being targeted by the IAVs, epithelial cells are also the first contacting sites for the inhaled IAV-laden droplets. The adaptive immune system (AIS) activation occurs in the lymphoid structure of the pulmonary system carried by the extra-pulmonary lymphatic vessels. Handel, Longini, and Antia (2007) studied the *in silico* IAV infection in humans and provided a model with seven variables for the virus, cell, and the combination of IIS and AIS. The parameter optimizations was performed by fitting the virus titer experiments. In Handel et al. (2007) model, the uninfected cells were controlled by the infection rate and were decreased by a death rate, i.e., a

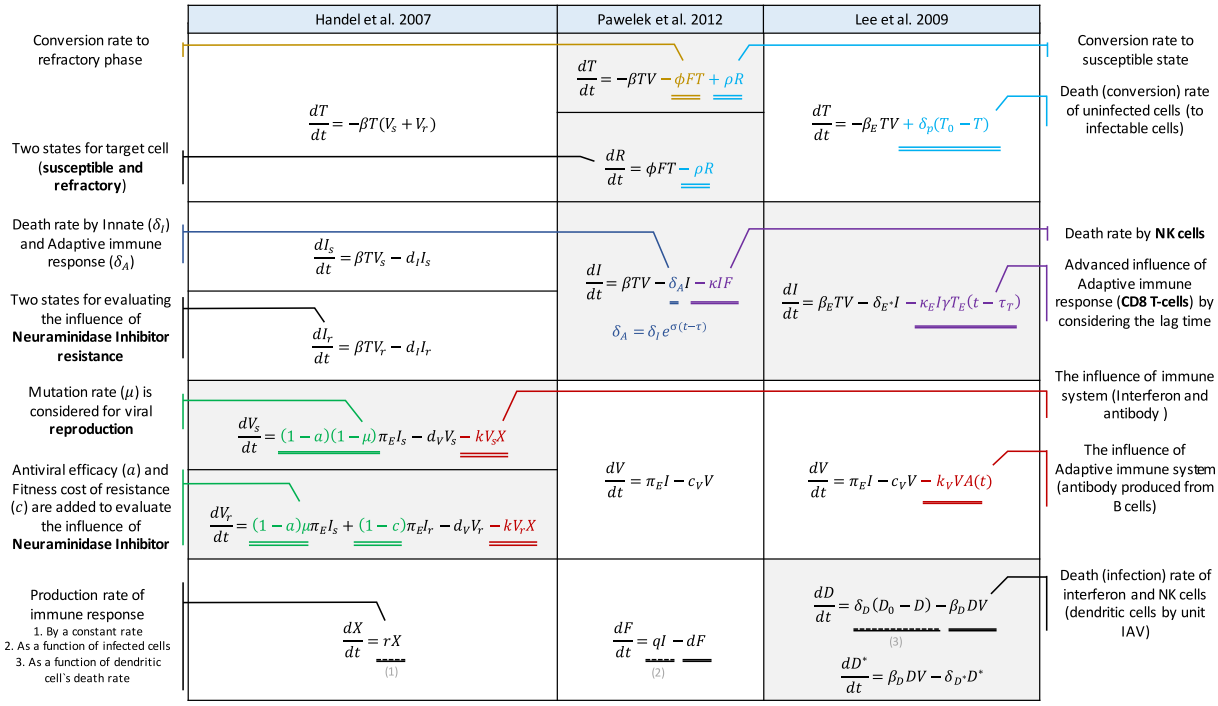

Fig. 2. Comparisons of existing IAV infection HCD models (Handel et al., 2007; Lee et al., 2009; Pawelek et al., 2012).

factor of the lag time and the initial immune response. The inclusion of the IIS in the HCD model was proposed by Pawelek et al. (2012). The target cells conversion to the refractory state, i.e., cells that become refractory to infection, was represented by the infection decreasing the frequency and the rate of antiviral release. The production of infected cells was presented by the rate of infection subtracted from the response from the NK cells. A constant AIS response rate was assumed before the emergence of AIS agents and then was exponentially increased to the maximum response. The virus growth rate was determined by the rate of change from the susceptible phase to the infected state, i.e., interfered by an increase in the population of (IFN)-I cytokines. Moreover, a simplified action of infected cell cytolysis by NK was introduced by considering a mass action term. The model proposed by Lee et al. (2009) showed the effect of AIS with considering dendritic cells as the intermediate agent between IIS and AIS. The similarity and incongruity of the three models are provided in Fig. 2.

In this study, the features of early HCD models (Handel et al. (2007); Pawelek et al. (2012); Lee et al. (2009)) are critically reviewed, combined, and optimized (see Table 1 for the underlying processes). The current HCD model variables and parameters are stated with underbars to be differentiated from the CFPD variables and parameters. The schematic of the interactions in host cells is presented in Fig. 1.

After inhaled IAV-laden droplets touch epithelial cells ($\underline{T}^T$), viral reproduction process starts immediately. By the secretion of interferons ($\underline{F}$), the neighboring epithelial cells become refractory ($\underline{R}$) to the infection. The virus titer ($\underline{V}$) and the infected cell ($\underline{I}$) count are connected by the rate of virus replication ($\underline{\beta}_E$). Targted cells ($\underline{T}_T$)are infected at the rate of $\underline{\beta T}_T\underline{V}$ and are converted to two

Table 1
The variable list for host cells, pathogen, IIS and AIS agents of the current HCD model.

Target Cells Refractory Cells	$\frac{d\underline{T}_T}{dt_H} = -\underline{\beta}_T \underline{T}_T \underline{V} - \underline{\phi}\underline{F}\underline{T}_T + \underline{\xi}_R \underline{R}\frac{d\underline{R}}{dt_H} = \underline{\phi}\underline{F}\underline{T}_T + \underline{\xi}_R \underline{R}$
Infected Cells	$\frac{d\underline{I}}{dt_H} = -\underline{\beta}_T \underline{T}_T \underline{V} - \underline{\kappa}_F \underline{I}\underline{F} - \underline{\kappa}_E \underline{I}\underline{\gamma}\underline{T}_C - \underline{\delta}_X \underline{I}\begin{cases}\underline{\delta}_X = \underline{\delta}_I t_H < \underline{\tau}_A \\ \underline{\delta}_X = \underline{\delta}_I e^{\underline{\sigma}(t_H - \underline{\tau}_A)} t_H > \underline{T}_A\end{cases}$
Virus	$\frac{d\underline{V}}{dt_H} = \underline{\beta}_E \underline{I} - \underline{\delta}_V \underline{V} - \underline{\kappa}_V \underline{VA}$
Dendritic Cells	$\frac{d\underline{D}_M}{dt_H} = \underline{\beta}_D \underline{D}_M(1 - \underline{D}_M/\underline{K}_D)\underline{V} - \underline{\delta}_D \underline{D}_M$
Helper T Cells	$\frac{d\underline{T}_H}{dt_H} = [\underline{\pi}_{H2}\underline{D}_M/(\underline{\pi}_{H2} + \underline{D}_M)](1 - \underline{T}_H/\underline{K}_H) - [\underline{\delta}_{H2}\underline{D}_M/(\underline{\delta}_{H2} + \underline{D}_M)]\underline{T}_H$
Cytotoxic T Cells B Cells	$\frac{d\underline{T}_C}{dt_H} = [\underline{\pi}_{C1}\underline{D}_M/(\underline{\pi}_{C2} + \underline{D}_M)](1 - \underline{T}_C/\underline{K}_C) - [\underline{\delta}_{C1}\underline{D}_M/(\underline{\delta}_{C2} + \underline{D}_M)]\underline{T}_C \frac{d\underline{B}}{dt_H} = \frac{\underline{\pi}_{B1}[\underline{D}_M + \underline{h}(\underline{V} + \underline{T}_H)]}{\underline{\pi}_{B2} + \underline{D}_M + \underline{h}(\underline{V} + \underline{T}_H)}(1 - \underline{B}/\underline{K}_B) - \underline{\delta}_B \underline{B} - \underline{\pi}_A \underline{B}$
Antibody	$\frac{d\underline{A}}{dt_H} = \underline{\pi}_A \underline{B} - \underline{\delta}_A \underline{A}$
Interferon	$\frac{d\underline{F}}{dt_H} = \underline{\beta}_F \underline{I} - \underline{\kappa}_A \underline{F}$

states of $\underline{R}$ and susceptible ($\underline{T}_T$) which is controlled by the production of $\underline{F}$, represented as $\underline{\pi}\underline{FT}_T$. In addition, to enhance the reverse action, a rate is introduced for conversion back to the susceptible phase ($\underline{\zeta}_R\underline{R}$). The effect of NK cells is incorporated into the interfering action of $\underline{F}$ as $\underline{\kappa}_F IF$. The influence of cytotoxic CD8$^+$ T cells is represented by defining the time of emergence ($\underline{\tau}_A$) and the migration factor ($\underline{\gamma}$). Other unknown sources of IIS and AIS responses are added to the infected cell equation ($\underline{\delta}_X\underline{I}$) with a constant value (δ_I) for IIS and a transient parameter with the growth rate of $\underline{\sigma}$ for the AIS. The $\underline{V}$ production rate is represented as $\underline{\beta}_E$ and the death rate of infection is defined by δ_V. Also, the effect of the antibodies ($\underline{A}$), i.e., produced by the mature B cells, on the virus reproduction deactivation is represented by the rate of ($\underline{\kappa}_V$).

Subsequently, the $\underline{D}_M$ processes antigen and present it on the AIS components. The critical agents simplify the AIS actions, i.e., CD8$^+$ T cell ($\underline{T}_C$), CD4$^+$ T cell ($\underline{T}_H$), and B cell ($\underline{B}$). The activation of the AIS components is considered as a function of the dendritic cell ($\underline{D}_M$) count (Lee et al., 2009). The CD8$^+$ T cell starts the apoptosis of infected cells and B cell generates the antibodies to stop the functionality of the virus with T helper cells. Logistic growth is selected for the operation of AIS components and the maximum values for the logistic profiles are adapted from the study by Lee et al. (2009) and compared with the predicted profile for the human infection by Handel et al. (2007). Finally, the antibody and interferon population balance are presented by considering a growth rate ($\underline{\pi}_A$ and $\underline{\delta}_A$, respectively) and death rate ($\underline{\beta}_F$ and $\underline{\kappa}_A$, respectively) for each of them.

The optimized parameters with detailed description and the reported data from previous works are provided in Table 2. Some of the parameters lack the physical meanings and the optimization variables were set up with the range of 1e-2 to 1e+3 compared to the data reported in the previous studies. Genetic Algorithm (GA) is used to optimize the HCD mathematical system with a vast number of constraints. GA classifies under probabilistic optimization algorithm which characterized as methods that encounter with the complicated and nebulous relation between a solution and its fitness (Weise, 2009). The evolution usually starts from a population of randomly generated individuals. The fitness of every individual is evaluated, and the best individuals are selected from the current population. As the next step, each genome is modified by replacing one or more individuals with new solutions, which are created either by combining two individuals (i.e., crossover) or by changing an individual (i.e., mutation) to form a new generation (Edgar, Himmelblau, & Lasdon, 2001). Practically, by considering the appropriate generation, the population explorer of the possible domain of an optimal solution is obtained. In this research, non-sorting genetic algorithm II (NSGAII) is selected to solve the developed optimization problem. Based on the results of the non-sorting genetic algorithm, Pareto-front is developed, and a single set of parameters is selected based on developed Pareto-front and the Technique for Order of Preference by Similarity to Ideal Solution (TOPSIS) as an efficient decision-making method. The objective is to minimize the absolute error between the experimental data and the HCD model for the viral titer and the IFN count (see Section 5.2). Optimized parameters, i.e., at the biologically feasible range, are changing regarding each other and the data probing has been investigated on the global domain. The optimization and decision-making processes are executed using MATLAB ("optimtool") and an in-house 4th-order Runge-Kutta method ODE solver.

4. Numerical setup

4.1. Geometry

As shown in Fig. 1, the subject-specific upper airway geometry excluding the nasal cavity was reconstructed from the Magnetic Resonance Imaging (MRI) scanned data (Zhang, Kleinstreuer, & Hyun, 2012b). In addition, the nasal cavity geometry acquired from the MRI scanned data set by Guilmette, Wicks, and Wolff (1989) contains two passages, which are separated by the nasal septum and merged at the posterior nasal aperture. The two geometries were connected at the soft palate between nasopharynx and oropharynx. Therefore, the upper airway, starting from the nares to Generation 6 (G6) was modeled as a single connected flow domain. To avoid unrealistic reverse flows adjacent to the airway outlets, extended tubes were added to all outlets.

4.2. Initial and boundary conditions

4.2.1. The CFPD model

As the two representative breathing patterns, mouth breathing (MB) and nasal breathing (NB) were considered and compared in this study. Realistic breathing waveforms were assigned as customized mouth inlet boundary conditions using UDFs. The transient volumetric flow rate data set were obtained from Scheinherr et al. (2015) for MB and Rennie et al. (2011) for NB. Both profiles represent the breathing patterns of healthy human subjects at rest. For the MB waveform, an 8-term Fourier series was used to fit the experimental data (see Fig. 3 (b) and Table 3 (a)). For the NB waveform, two 7-term sinusoidal function series were used to fit the breathing profile data at left and right nostrils separately (see Fig. 3 (a) and Table 3 (b)).

For the sneezing event, the number and diameter of dispersed droplets in the expelled aerosol were acquired from Duguid (1946). The droplet size distribution was divided into 6 bins that encompass droplet diameters from 1 to 100 μm. The time duration (t_{exp}) and the peak volumetric flow rate (Q_{exp}) of expelled IAV-laden droplets carried by the airflow are defined as 0.7 s (Han, Weng, & Huang, 2013) and 21.5 L/s (Scharfman, Techet, Bush, & Bourouiba, 2016), respectively. A 1 meter high circular cone was used to estimate the total aerosol volume (V_{dis}) at the time that the subject starts to be in contact with the expelled IAV-laden droplets from the infected subject. Specifically, the vertex of the cone is at the mouth/nose region of the infected subject, and the axis of the cone is assumed to be parallel to the ground. The properties of the IAV-laden droplets and the initial and boundary conditions for the CFPD model are given in Table 4.

Table 2
Optimized parameters of the HCD model.

Parameter	Definition	Reference Values	Optimized Value
β_T	Infection rate	9.9e-2[a] ml/day.$TCID_{50}$ 4.7e-5[b d] (RNA copy)$^{-1}$ml NS day^{-1} 7e-5[c] day^{-1}(EID_{50}/ml)$^{-1}$	9.89e-3
ϕ	IFN-induced antiviral efficacy	3.3e-1[b d] (IFN fold change)$^{-1}$day^{-1}	5.01e-1
ζ_R	Reversion rate from refractory	2.6[b d] day^{-1}	1.15
κ_F	Killing rate of infected cells by NK cells	4.2[b d] (IFN fold change)$^{-1}$day^{-1}	1.24e-2
κ_E	Killing rate of infected cells by CD8$^+$ T cells	1.19e-3[c] day^{-1}	1.29e-2
γ	CD8$^+$ T cells migration factor	0.15[c]	0.925
δ_I	The death rate of infected cells	5.0e-1[a] day^{-1} 2[b] day^{-1} 1.2[c] day^{-1}	5.02e-1
σ	Death rate increases factor	0.99[b d]	0.98
τ_A	Time at which AIS become fully functional	4.87[b d] day	1.5
β_E	Virus production rate	1.2e-5[a] $TCID_{50}$day^{-1}ml^{-1} 5.3e-3[b d] RNA copies (ml NS)$^{-1}$day^{-1}cell^{-1} 1.9 EID_{50}day^{-1}ml^{-1}	1.80e-5
δ_V	Clearance rate of free virions	8.1e-2[a] day^{-1} 15[b d] day^{-1} 1[c] day^{-1}	9.85e-1
κ_V	Rate of IAV neutralization by unit anti-IAV antibody	4e-3[c] day^{-1}titer^{-1}	6e-3
β_D	The infection rate of Dendritic cells by unit IAV	1e-2[c] day^{-1}(EID_{50}/ml)$^{-1}$	1.04e-2
K_D	Max. value of the Dendritic cells	1e+5[c]	1e+5
δ_D	The death rate of mature dendritic cells	5e-1[c] day^{-1}	10e-1
π_{H1}	Max. activation rate of naïve CD4$^+$ T cells	1.5[c] day^{-1}	1.85
π_{H2}	No. of Dendritic cells for half-maximal activation of naïve CD4$^+$ T cells	1e+2[c]	1e+2
K_H	Max. value of the activated CD4$^+$ T cells	1e+5[c]	1.1e+5
δ_{H1}	Max. clearance rate of effector CD4$^+$ T cells	4e-1[c] day^{-1}	0.48
δ_{H2}	No. of Dendritic cells for half-maximal clearance of effector CD4$^+$ T cells	1[c]	1
π_{C1}	Max. activation rate of naïve CD8$^+$ T cells	3[c] day^{-1}	2.94
π_{C2}	No. of Dendritic cells for half-maximal activation of naïve CD8$^+$ T cells	1e+2[c]	9e+2
K_C	Max. value of the activated CD8$^+$ T cells	1e+5[c]	1e+5
δ_{C1}	Max. clearance rate of effector CD8$^+$ T cells	75e-2[c] day^{-1}	0.95
δ_{C2}	No. of Dendritic cells for half-maximal clearance of effector CD8$^+$ T cells	1[c]	1
π_{B1}	Max. activation rate of naïve B cells	3[c] day^{-1}	3.02
π_{B2}	No. of Dendritic cells for half-maximal activation of naïve B cells	1e+4[c]	1e+4
K_B	Max. value of the activated B cells	1e+5[c]	1e+5
δ_B	The clearance rate of activated B cells	9e-1[c] day^{-1}	0.9
π_A	The secretion rate of antibody titer by unit short-lived plasma cell	6e-2[c] day^{-1}	0.9
δ_A	The clearance rate of antibody	4e-2[c] day^{-1}	4e-3
β_F	The production rate of IFN	9.6e-10[b d] (IFN fold change) day^{-1}cell^{-1}	6.20e-7
κ_A	The decay rate of IFN	1.9[b d] day^{-1}	4.6e-1

[a] Handel et al., 2007.
[b] Pawelek et al., 2012.
[c] Lee et al., 2009.
[d] Avg values reported by Pawelek et al., 2012.

4.2.2. The HCD model

For the HCD model, initial conditions were obtained from early studies (see Table 5). For estimating the epithelial cell population at each region, the mean cell size of 2.5e-7 cm^3 reported by Farmer (1991) is considered. To obtain eligible inputs from the lung deposition data predicted by the CFPD model for the post-deposition analysis, the number of inhaled IAV-laden droplets that can represent one 50% tissue culture infectious dose ($TCID_{50}$) need to be determined. The biological decay of the IAV-laden droplet is also considered in the modeling process. Tellier (2009) showed 150–650 RNA copies of IAV represent 1 $TCID_{50}$. Yang, Elankumaran, and Marr (2011) had an estimated 2,100 and 452 genome copies per $TCID_{50}$ of A/PR/8/34 (H1N1) and A/California/04/2009 (H1N1) strains, respectively. On average, the results showed the 1-hour exposure to 1.6e+4 genome copies per m^3 represents 35.4 ± 21.0 $TCID_{50}$ per m^3. In this study, the experimental data by Ward et al. (2004) is used, which shows that 1 $TCID_{50}$ ml^{-1} holds 1000 copies of the viral genome and also each viral particulate ($d_d^0 < 1$ μm) was expected to hold 1 viral agent (Knight, 1980).

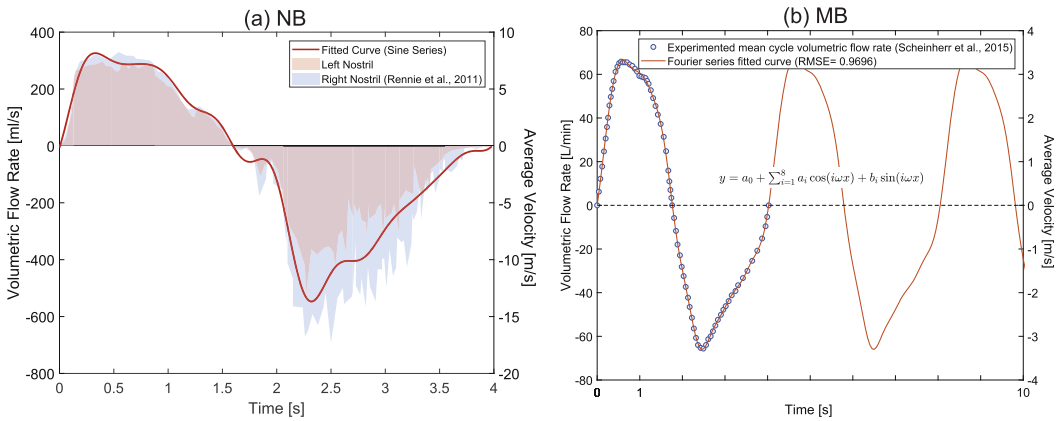

Fig. 3. Subject-specific nasal and mouth breathing patterns. (a) NB at each nostril: the average data is collected and is fitted with the summation of sines with 7-term; (b) MB is fitted with 8-term Fourier series.

Table 3
Fitted equations for the realistic breathing patterns (MB and NB).

(a)Mouth Breathing		
Fourier Series with 8 Terms $Q = a_0 + \sum_{i=1}^{8} a_i \cos(iwt) + b_i \sin(iwt)$		
i	a_i	b_i
0	−1.462	0
1	19.55	60.38
2	−10.90	−0.9638
3	−1.6	7.435
4	−2.737	1.096
5	−2.057	−0.4919
6	−0.4734	0.7077
7	−0.4042	−0.8452
8	0.08115	0.6936
W = 1.561		

(b) Nose Breathing			
Sum of Sines with 7 Terms $Q = \sum_{i=1}^{7} a_i \sin(b_i t + c_i)$			
i	a_i	b_i	c_i
1	263.7	0.6369	3.015
2	330.7	0.1254	−3.727
3	73.19	4.86	−0.7755
4	48.58	7.822	−0.7588
5	16.06	13.33	0.03013
6	253.6	2.011	−0.4039
7	43.69	10.85	−1.085

5. Model validations

5.1. CFPD model validations

The CFPD model has been well validated in early studies by the airflow field and regional particle deposition comparisons with benchmark experimental data (Feng et al., 2018; Haghnegahdar, Feng, Chen, & Lin, 2018). The advanced DPM modeling capability in this study, i.e., the accuracy of droplet size change dynamics prediction, is extensively validated. The validation was done by comparing the size changes of two different scenarios of dilute aqueous droplet evaporation and a dry NaCl particle condensation with experimental data (El Golli, Arnaud, Bricard, & Treiner, 1977; Li, Montassier, & Hopke, 1992).

Specifically, for validating the droplet evaporation, the simulation results were compared with the experimental data by El Golli et al. (1977). Fig. 4 (a) shows the influence of the initial compositions of the droplet on its evaporation and the comparison of the

Table 4
IAV-laden droplet properties in the expelled aerosol by sneezing and the initial and boundary conditions for the CFPD model.

Sneezing Event	Distribution Bins (Duguid, 1946)	Droplet Diameter (d_d) [μm]	Number of Expelled Droplets
		1–2	26,000
		2–4	160,000
		4–10	420,000
		10–25	26,000
		25–50	58,375
		50–100	14,500
		+100	fall to the ground and not able to be airborne
	t_{exp} [s]	0.3–0.7	Han et al. (2013)
	Q_{exp} [L/s]	21.5	Scharfman et al., 2016 (from the Reynolds number)
Properties	Droplet Density f(T_d, Y_{NaCl})	Correlation	Simion, Grigoraş, Roșu, and Gavrilă (2015)
	Diffusivity f(T)	Correlation	Treybal (1980)
	Surface Tension f(T_d, Y_{NaCl})	Correlation	Weissenborn and Pugh (1996)
	Mean Free Path [m]	9.85E-08	air-water vapor
	Inlet Temperature [K]	310.15	
	RH [%]	Inlet Airflow: 40	Airway Walls: 99.5
Regional Surface Area [m^2]	Oral Cavity	4.61E-03	
	Oral Cavity	1.37E-02	
	Oropharynx	2.21E-03	
	Nasopharynx	1.56E-03	
	Glottis	5.00E-03	
	Trachea	6.66E-03	
	Airways (G1-G6)	4.25E-02	

Table 5
Initial conditions and simulated variable definitions of the HCD model.

Variable	Definition	Initial Value [unit]
$\underset{\sim}{T}_T$	Uninfected epithelial cells	4e+8[a] [cells]
$\underset{\sim}{R}$	Epithelial cells in the refractory state	0[b] [cells]
$\underset{\sim}{I}$	Infected epithelial cells	0[a] [cells]
$\underset{\sim}{V}$	Virus titer	Regional deposition from the CFPD model 5 [$TCID_{50} ml^{-1}$]
$\underset{\sim}{D}_M$	Mature dendritic cells	1e+3[c] [cells]
$\underset{\sim}{T}_H$	Effector $CD4^+$ T cells	0[c] [cells]
$\underset{\sim}{T}_C$	Effector $CD8^+$ T cells	0[c] [cells]
$\underset{\sim}{B}$	Activated B cells	0[c] [cells]
$\underset{\sim}{A}$	Antiviral antibody titer	110.2[c] [titers]
$\underset{\sim}{F}$	Interferon	10[d] [IFN fold change]

[a] Handel et al., 2007.
[b] Pawelek et al., 2012.
[c] Lee et al. (2009).
[d] Fritz et al., 1999.

CFPD modeling results with the experimental data. Droplets were injected with the initial diameter of 16 μm to the airflow stream with the relative humidity RH = 70%. Specifically, water-NaCl droplets with different molalities (m = mol/kg) are simulated and visualized. Fig. 4 (b) further shows the influence of the ambient RH, the initial droplet diameter, and the initial NaCl molality in droplets on the evaporation characteristics. Specifically, it can be observed in Fig. 4 (b) that the increase in ambient RH will reduce the initial water partial pressure gradient for evaporation cases, thereby lower the initial evaporation rate of the droplets. Good agreements can be found in Fig. 4 (a) and (b) between the CFPD modeling results and the experimental data, indicating the reliability of the CFPD model to predict droplet evaporation dynamics accurately. For validating the condensation on droplets, the simulation results were extensively compared with the experimental data by Li et al. (1992). Fig. 4 (c) shows the comparison of the droplet hygroscopic growth rate versus the initial droplet diameter with various airflow RH and temperature. For the dry NaCl particle simulations, the initial diameter d_d^0 is equal to 200 nm released into the domain with RH = 99.5% and T = 295.15 K. Specifically, a small increase in RH (from 99% to 99.5%) resulted in a substantial increase in the droplet size growth. The agreement between the numerical and experimental data is acceptable and the differences are due to the experimental errors on controlling the ambient RH.

5.2. HCD model validations

The validation of the HCD model was executed by comparing the HCD simulation data with the viral titer of the IAV H1N1 infection by Fritz et al. (1999); Hayden et al. (1998) as well as the average IAV H3N2 viral titer data provided by Hayden et al. (1996)

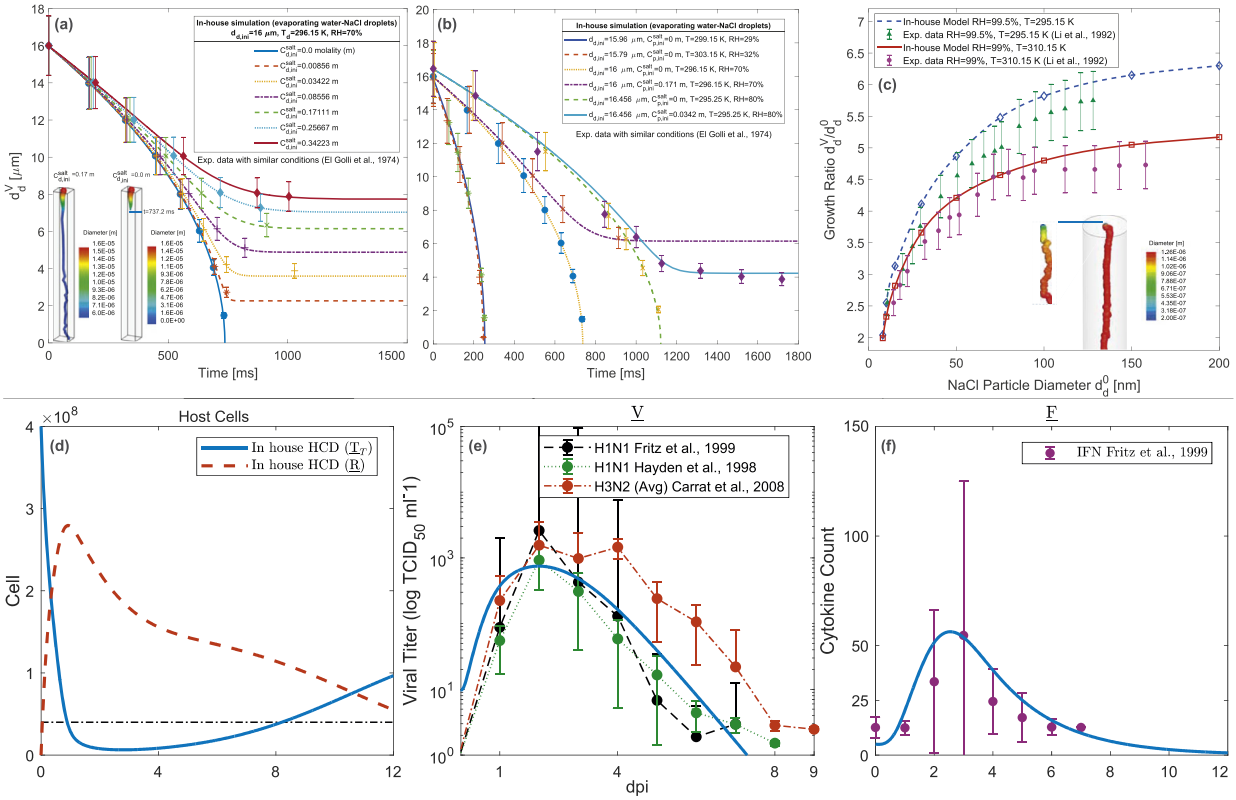

Fig. 4. The CFPD-HCD model validations: (a-b) Droplet dynamics validation at different molality (m), RH, and T (El Golli et al., 1977); (c) The validation of dry NaCl particle hygroscopic growth at different RH and T; (d) In-house HCD modeling results of the concentration time courses for the targeted cell, infected cell, and refractory cell; (e) Comparisons of the mean viral titer [$TCID_{50}\ ml^{-1}$] for the HCD model validation; and (f) Comparisons of the IFN data in early studies Fritz et al. (1999); Hayden et al. (1998, 1996).

(Fig. 4 (f)). Furthermore, the Interferon (IFN) data by Fritz et al. (1999) was also used to validate the prediction of IFN time courses (Fig. 4 (f)). Fig. 4 (e) shows the viral titer data for $TCID_{50}$/ml of nasal wash. One $TCID_{50}$ corresponds to a single infectious virion (Handel et al., 2007). The initial value of the virus titer is considered as 5 (Lee et al., 2009) (see Table 5). Fig. 4 (d) shows the predicted HCD for the target and refractory cells. The numerical time courses match the experimental data well, which provides direct evidence for the HCD model validation.

6. Results and discussion

6.1. Airflow field

Figs. 5 and 6 show the volume renderings of the normalized airflow velocity magnitude ($\|\vec{V}\|$) and velocity distributions at the multiple cross-sections. The normalization for the NB case was done via dividing the velocity magnitude by $\|\vec{V}_{max}\| = 23.5$ m/s, which is at the time of peak exhalation (t = 2.35 s) at the inferior nasal aperture both in the left and right nasal passages. For the MB case, the normalization was done via dividing the velocity magnitude by $\|\vec{V}_{max}\| = 14.5$ m/s which is at t = 0.56 s on the onset of the epiglottis and the laryngeal jet cores.

For the NB case, the mainstream $\|\vec{V}\|$ distributions are visualized at 6 cross-sections and the secondary flows are shown by in-plane streamlines and velocity vectors (see Fig. 5). In Fig. 5, the top row shows the results at the time when the peak inspiratory velocity (t = 0.35 s) is reached, and the bottom row shows the results at the peak exhalation (t = 2.35 s). Nasal inlet jets are hitting the superior conchae and the resultant lower pressure next to the inferior concha drives the secondary flow and clockwise (CW) vortices at cross-section A (Fig. 5 (a)-A). At t = 0.35 s, the Reynolds number (Re) at the right nostril is 3,695 and recirculation zones are formed in the cavity between the inferior turbinate and the nasal septum. Moving forward in the nasal passages, the middle turbinate appears which changed L-shaped passage (see Fig. 11 (a)-A) to Y-shaped (see Fig. 11 (a)−B) spacing. The flow was separated into three fissures. The pressure drop at the cavity next to the bifurcating point of the Y-shaped opening caused the recirculations to form, i.e., CW in the left passage and counter-clockwise (CCW) in the right passage (Fig. 5 (a)-B). Towards the posterior nasal apertures, the two passages deform to ξ-shaped passages when superior turbinate appears and the recirculation intensities were dissipated (Fig. 5 (a)-C). The two passages merge into the nasopharynx. The velocity vectors showed the backward direction as the merged flow from

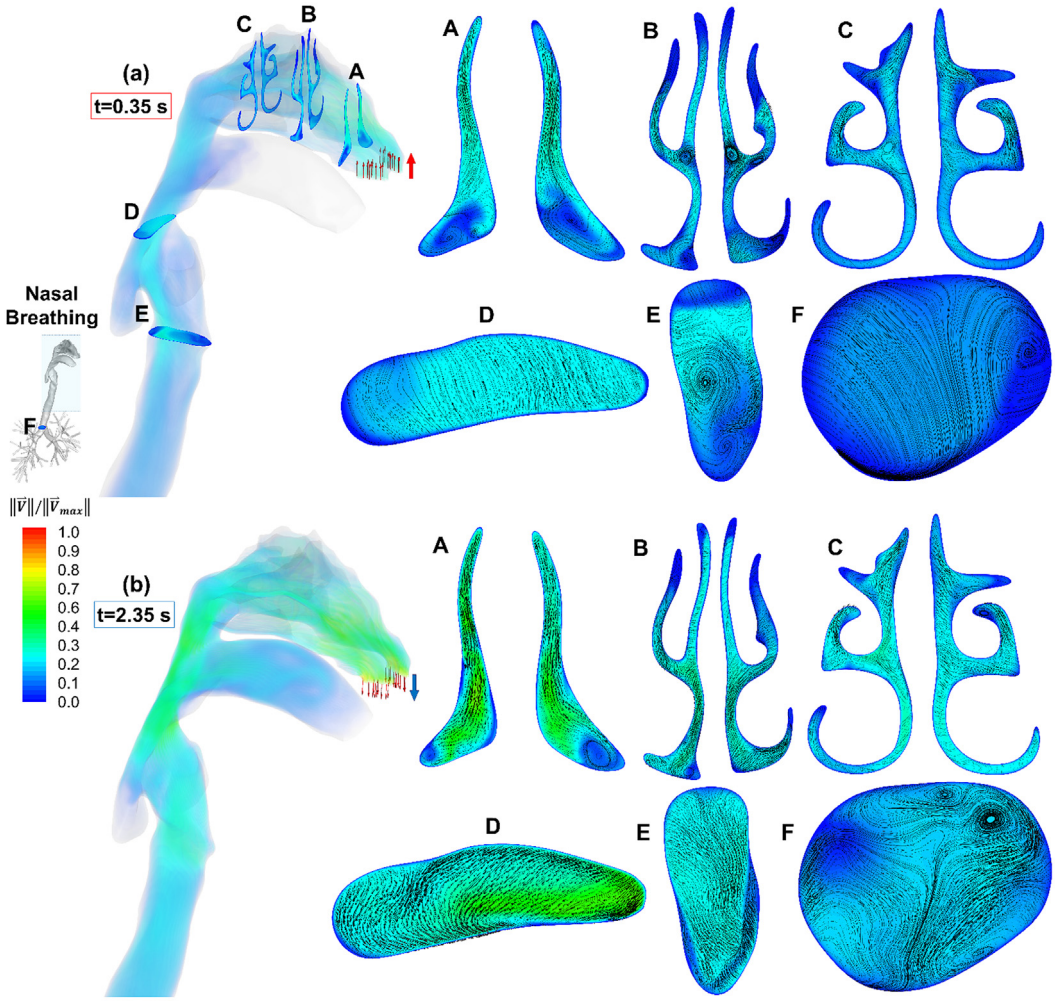

Fig. 5. Airflow velocity contours and volume rendering in the human respiratory system at t = 0.35 s (the peak inspiratory velocity) and t = 2.35 s (the peak expiratory velocity) for the NB case.

the nasal cavity hits the posterior wall of the oropharynx (Fig. 5 (a)-D). The same patterns exist until the mainstream airflow enters the trachea. At the glottis, due to the pressure drop at the dead volumes of the laryngopharynx (piriform recesses) a CCW recirculation region is formed (Fig. 5 (a)-E), being accompanied by the laryngeal jet. In the trachea, Re decreases from 2,628 at the glottis to 1,760 when reaching G1 which indicates the re-laminarization from the turbulence near the glottis (Fig. 5 (a)-D and F).

At the peak of nasal exhalation, the flow develops from airstream discharges from the lung and Re is 3,871 at cross-section F (Fig. 5 (b)-F). As a result, the incipient turbulence is expected. Vortices are formed, as the flow deviated to the anterior wall of the trachea (Fig. 5 (b)-F). As the expiratory flow reached the glottis, the turbulence intensity reduced and Re is 3,520. In the nasopharynx, the stream separated by uvula into two parts and headed toward the nasal and oral cavities. As the mouth is closed, static pressure differences at the mouth front generate resistance to the airflow entering the oral cavity, leading to the recirculating flow patterns shown by the volume rendering graph at t = 2.35 s. Following the flow in the nasal cavity, the superior section of the nasopharynx, i.e., where the pharyngeal tonsil is located, directed the airflow into the nasal passages.

Fig. 6 represents the velocity field at the time stations with the peak inhalation and exhalation flow rates, of the MB profile, i.e., t = 0.56 s and t = 2.48 s. It can be observed that the high-velocity jet core enters the oral cavity and stays near the lower palate. At t = 0.56 s, due to low static pressure near the central part of the lower palate, induced by the high-velocity airflow, two counter-rotating vortices are generated near the upper palate which are visualized at cross-section A (see Fig. 6 (a)-A). With the airflow progressing to cross-section B near the 90-degree bend between the oral cavity and pharynx, the triangular lower wall was deformed to a symmetrical geometry with a flat lower wall (Fig. 6 (a)-B). As a result, recirculations on the left side of cross-section B are extended and cause deviation the vortex core on the right side from the centerline. It also creates a CW vortex in the oropharynx and the mainstream moves further towards the right side at cross-section C. Passing the glottis, a laryngeal jet is formed and impacts the posterior side of the trachea. During the mouth exhalation phase shown in Fig. 6 at t = 2.48 s, the expiratory laryngeal jet was generated and touched the larynx. The maximum airflow velocity was generated at the constriction of the oropharynx (Fig. 6 (b)-C).

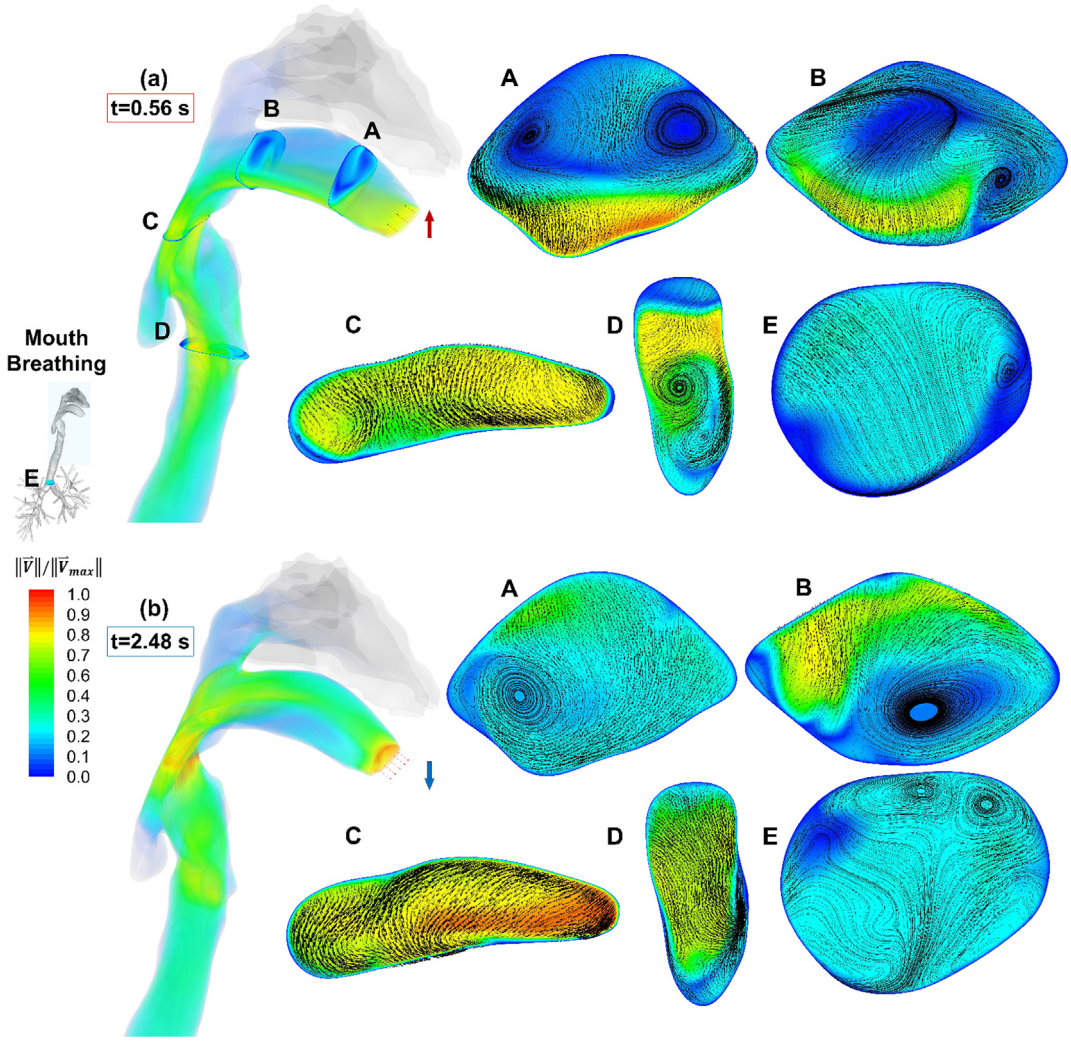

Fig. 6. Airflow velocity contours and volume rendering in the human respiratory system at t = 0.56 s (the peak inspiratory velocity) and t = 2.48 s (the peak expiratory velocity) for the MB case.

A portion of the flow entered the posterior nasal cavity, but was not able to penetrate further into the anterior portion. Such a phenomenon is due to the momentum loss of the airflow which failed to overcome the high resistance in the nasal cavity. In contrast to the observation that the high-velocity airflow is close to the lower palate during the mouth inhalation phase, part of the expiratory airflow entered the oral cavity and directly impacted the upper palate.

The comparison of the airflow fields between NB and MB cases indicate that the nasal passage can significantly reduce the airflow momentum at the post-nasal region. During the NB inhalation, the core of the laryngeal jet has lower turbulence strength that results in a weaker impaction of flow to the posterior tracheal wall compared to the MB case. As a result, lower inertial impaction and droplet deposition is expected for the NB case at the trachea. However, there are similarities between the flow pattern at the subglottal regions between the MB and NB. During the inhalation, the flow pattern at the mid-trachea is similar between MB and NB (see Fig. 5 (a)-E and 6 (a)-F). During the exhalation, the secondary flows at the mid-trachea and glottis are similar between NB and MB. The similarity of the flow patterns at the subglottal airways for both cases implies that the glottal contraction can re-regulate the airflow patterns and diminish the flow characteristics induced by different ways of breathing *via* mouth or nose, as well as the supraglottal anatomical variability.

6.2. Relative humidity (RH) distributions

The relative humidity (RH) is calculated by having the local temperature, pressure, and mass fraction of the water vapor. Fig. 7 shows the RH in percentage for both NB (the top row) and MB (the bottom row) cases. The contours are at the onset of inhalation (t = 0.10 s), the peak inhalation (t = 0.35 s for NB and t = 0.56 s for MB), and at the end of inhalation (t = 1.60 s for NB and t = 0.56 s for MB). The ambient water vapor mass fractions were determined based on the standard condition, i.e., T = 310 K and

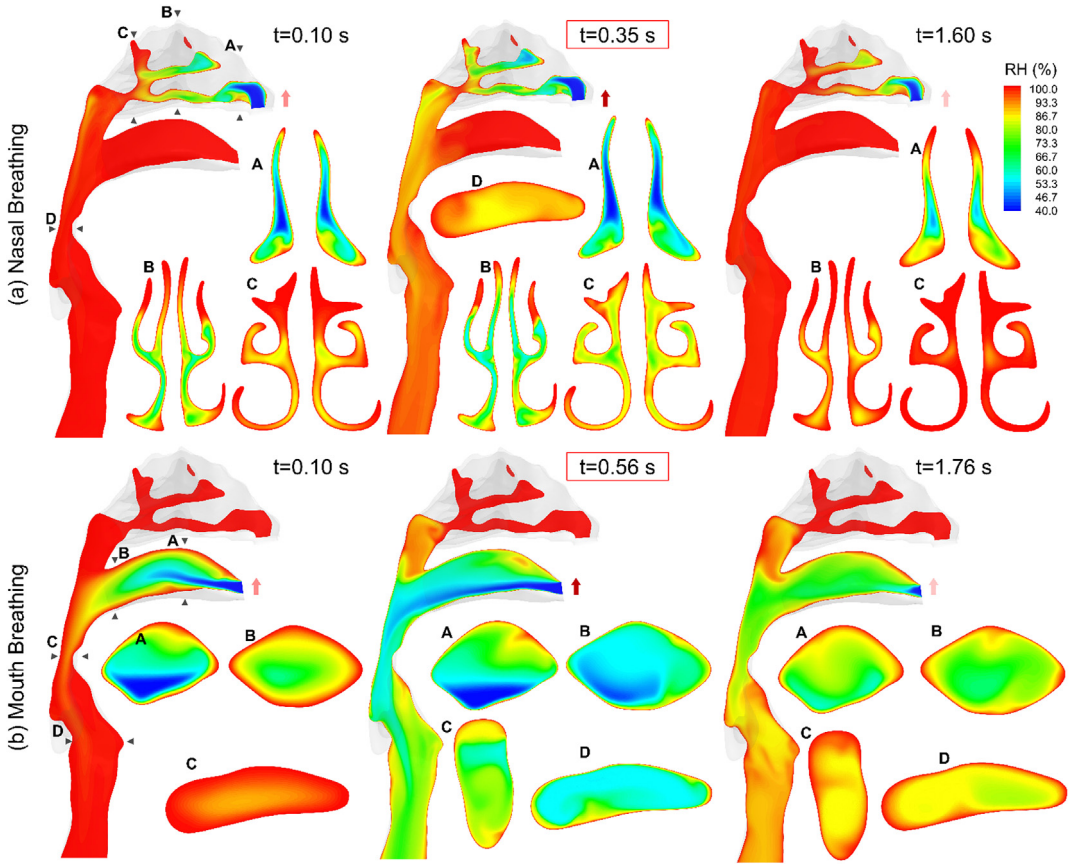

Fig. 7. Localized RH distributions of the respired humid air with RH = 40% during NB and MB at different time stations of inhalation.

RH = 40% at 1 atm. The initial RH in the human respiratory system is assumed to be constant and equal to 99.5% and the airway walls were considered nearly saturated at which RH = 99.5% (Ferron, 1977). Simulation results show that during the inhalation phase of NB, dry ambient air entering the nasal cavity started to lower the local RH. Due to the large ratio between surface area and passage length in the nose, high RH at the saturated airway walls can create sufficiently high gradients to compensate for the loss of water vapor. Therefore, at the peak inhalation flow rate (t = 0.35 s), RH is still higher than 90% from the nasopharynx to the mid-trachea. It can also be observed that the RH distributions are significantly influenced by the localized airflow patterns shown in Fig. 5. Specifically, The RH values in those recirculation regions are higher because of the longer residence time of the trapped dryer airs than those in the mainstreams. Additionally, because of the reduced convection effect at the end of nasal inhalation (t = 1.60 s), RH in the upper airways (shown in Fig. 7 (a)) recovers to 99.5% due to the dominant water vapor diffusion from the saturated airway walls to the bulk region in the nasal cavity. For the MB case at t = 0.10 s, the inhaled dry air stream has already influenced the entire oral cavity. As the flow impacts the lower palate, the low RH flow deviates towards the upper palate and reduced the localized water vapor mass fractions. At t = 0.56 s, i.e., the peak inhalation flow rate, the influence of dry air on the RH reaches the mid-trachea. Comparing with the velocity profile shown in Fig. 6 (a)-A, the recirculation zones created by the two vortices near the mouth front results in higher local RH values. In detail, the average RHs at oropharynx and glottis are 54.3% and 61.6%, respectively. At the end of inhalation for the MB case (t = 1.76 s), RH values in the upper airway did not recover as prompt as the NB case. Comparisons between NB and MB cases show that the inhaled airflow with lower RH can make the airway dryer with MB than with NB. The high ratio between the surface area and passage distance of the nasal cavity provide significant compensation of the humidity and restrict the influence of dry air more efficiently than the oral cavity.

6.3. Size change dynamics and deposition patterns of inhaled IAV-laden droplets

Fig. 8 shows the positions of suspending droplets at t = 1.6 s for NB and t = 1.76 s for MB, i.e., the time stations of the transitions between inhalation and exhalation. Three compositions of the water-NaCl droplets were investigated (see Section 2 for droplet compositions). In Fig. 8, droplets are colored based on their diameters. To visualize and compare droplet size change dynamics with better clarity, only droplets with an initial diameter equal to 7 μm are shown. For the inhalation of pure water droplets in the NB case, it can be observed that droplets were undergoing evaporation. Fast droplet size shrinkages happen in the nasal cavity, because of the lower regional RH (see Fig. 7 (a)). Specifically, based on the observation that the RH decreases in the nasal cavity during the

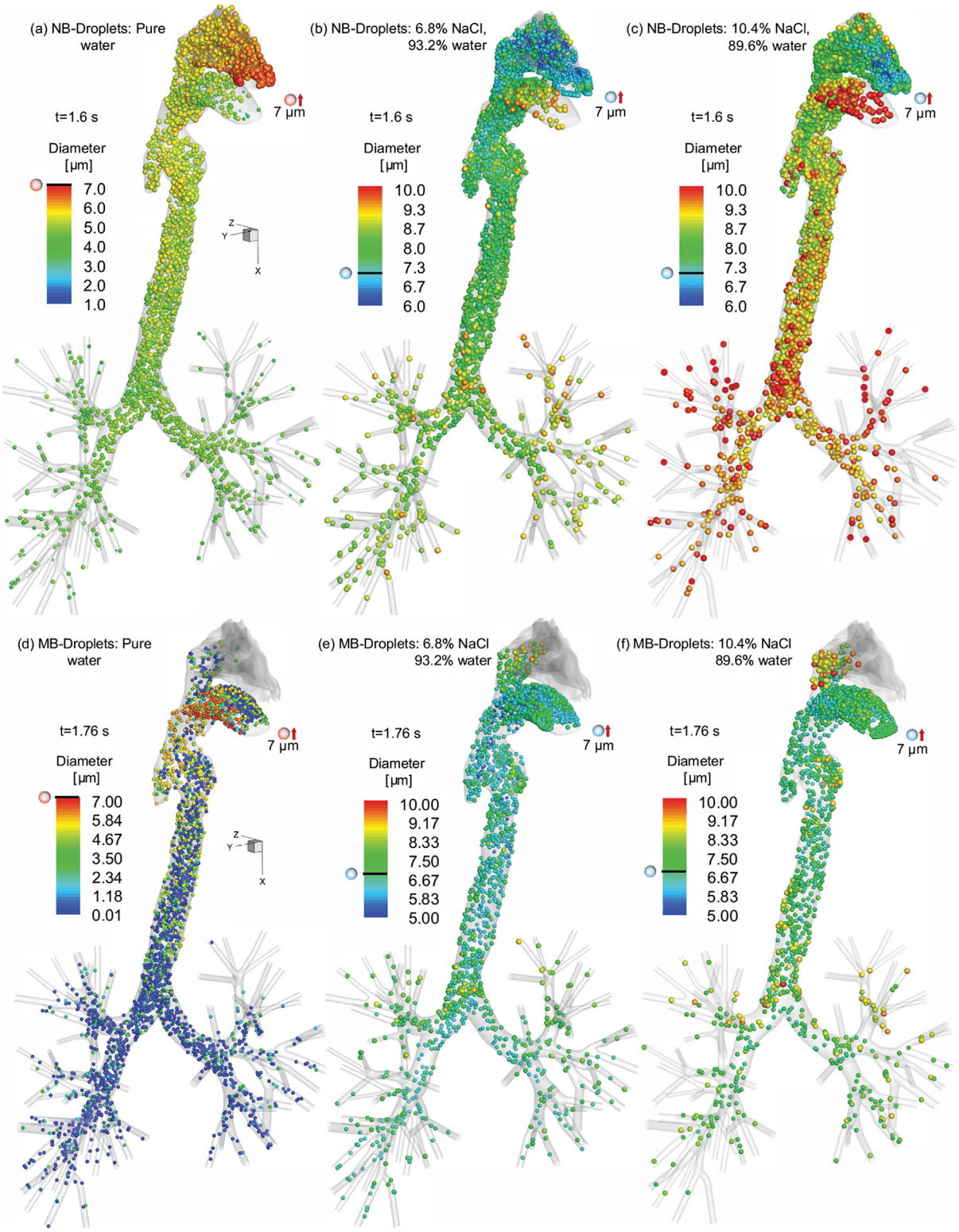

Fig. 8. The distribution of suspending droplets at t = 1.60 s for NB and at t = 1.76 s for MB (droplet initial diameter: 7 μm).

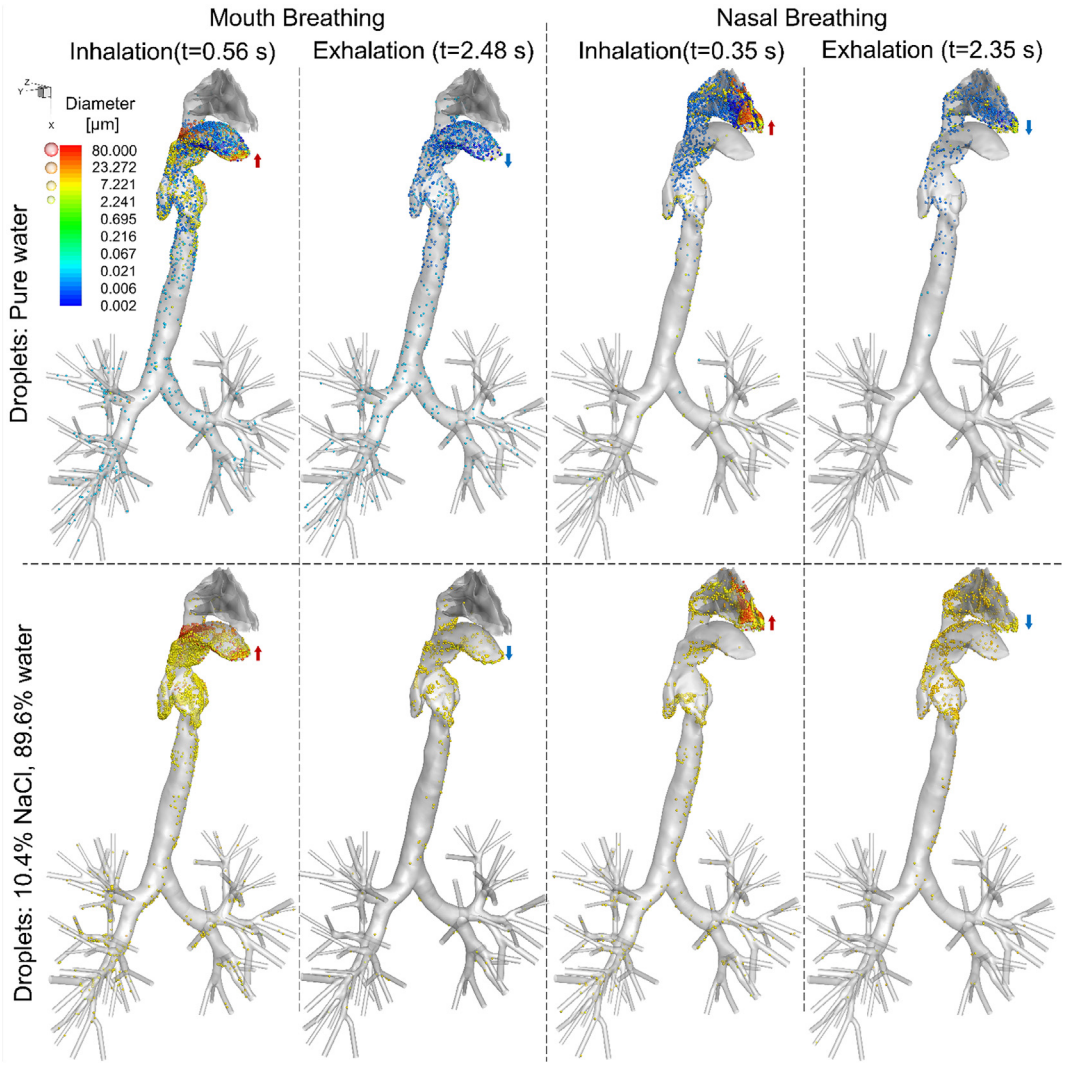

Fig. 9. Local deposition patterns of the pure water and isotonic aqueous droplets ($Y_{NaCl} = 10.4\%$) with polydispersed droplet injections at different time stations for the NB and MB cases.

inhalation phase of the NB cases, significant water evaporation occurs accordingly in supraglottal regions. In contrast, during MB inhalation of the pure water droplets, RH is much lower in the entire upper airway compared to the NB case. Therefore, evaporation in the mouth inhalation has higher rates due to the higher partial pressure gradients of water. Specifically, the highest mass exchange occurred in the oropharynx and continued in the trachea. As a result, lower droplet diameters can be observed in the MB case than the NB case (see Fig. 8 (a) and (d)).

For droplets containing 6.8% NaCl inhaled *via* NB (see Fig. 8 (b)), evaporation and the resultant decrease in droplet diameters can be observed near the nostrils. The size change dynamics is because the inlet jet increases the droplets Reynolds number and consequently the heat and mass transfer due to the higher *Sh* and *Nu*, respectively. Also, lower RH of the inlet flow resulted in an elevated mass exchange between the droplets and the surrounding gas mixture. With the droplets traveling into the high-RH regions, ambient water vapor started to condensate on droplets and initiated the hygroscopic growth. During the inhalation (see Fig. 8 (b)), some droplets entered and stayed in the nasal cavity with larger diameters than other droplets. Since droplets suspending in the domain has the same residence time, i.e., 1.6 s, such differences in size growth is due to the higher condensation mass rate induced by higher local RH in the nasal cavity (RH = 99.5%). A similar trend could be observed for the MB case on the transport of droplets with 6.8% NaCl (see Fig. 8 (e)). However, due to the lower RH distributions in the MB case compared with the NB case, the partial pressure gradient is smaller and the condensation rate is lower. Therefore, the average droplet size visualized is smaller than the NB case. For droplets with 10.4% NaCl, the high NaCl concentration lowered the water partial pressure and increased the concentration rate. Thus, the stronger hygroscopic growth happens for droplets with 10.4% NaCl than those with 6.8% NaCl (compare Fig. 8 (b) and (c) for the NB cases and Fig. 8 (e) and (f) for the MB cases).

Deposition patterns of droplets with different initial compositions are visualized in Fig. 9 for both the MB and NB cases. Droplets

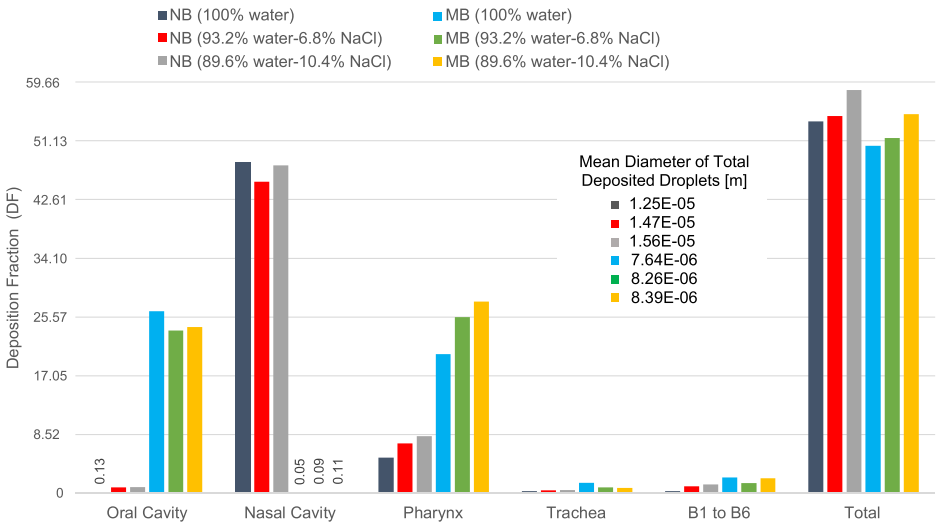

Fig. 10. Regional deposition fractions (RDFs) of droplets with different initial compositions colored by the mean diameter of deposited droplets.

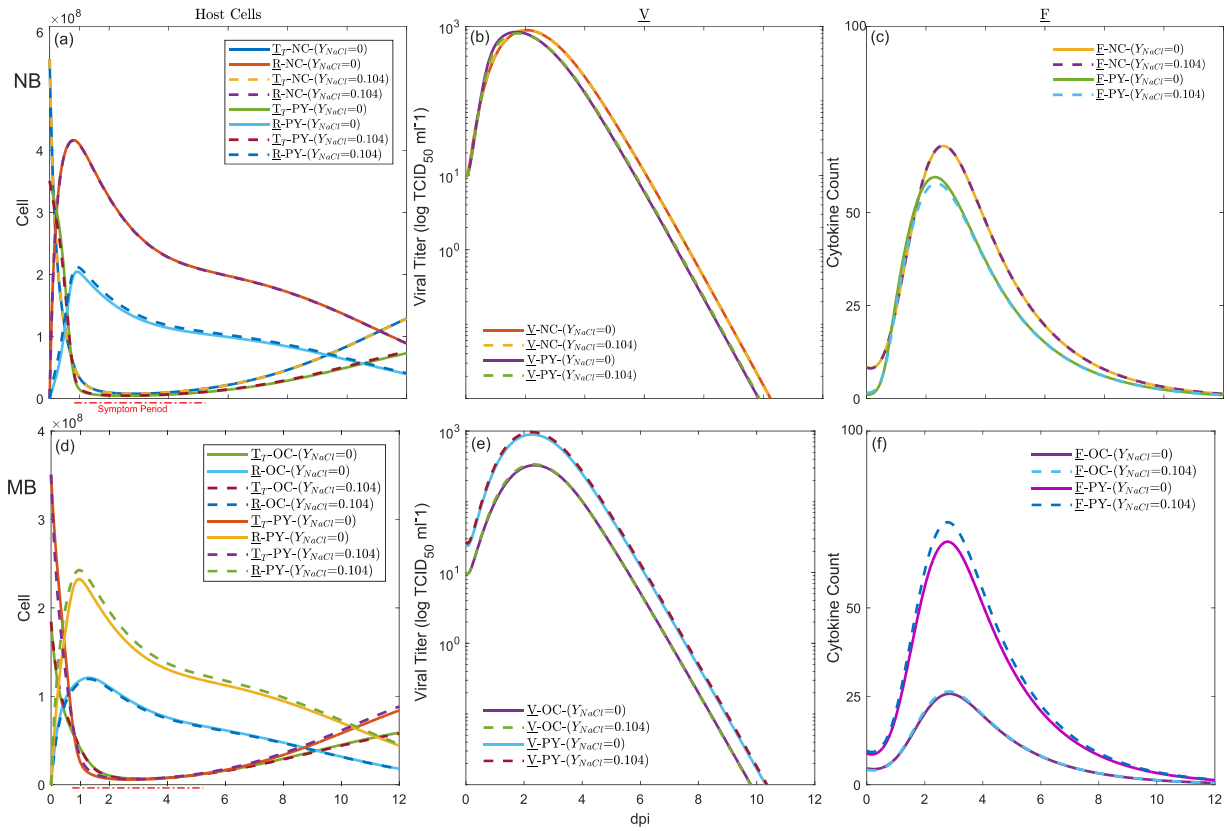

Fig. 11. Regional virus titer predictions using the CFPD-HCD model: (a-c) The HCD in the nasal cavity (NC) and the pharynx (PY) for droplets inhalation using the nose (NB) with different NaCl concentrations ($Y_{NaCl} = 0$ and $Y_{NaCl} = 0.104$); and (d-f) The HCD in the oral cavity (OC) and the pharynx (PY) for droplets inhalation using the mouth (MB) with different NaCl concentrations ($Y_{NaCl} = 0$ and $Y_{NaCl} = 0.104$).

are colored by their final diameters at deposition sites. During MB of the pure water droplets, 20–80 μm droplets deposit mainly at the back of the oral cavity and oropharynx due to dominant inertial impaction effect. Additionally, dispersed deposition patterns of nanoscale droplets can be found in the oral cavity due to the dominant influence of Brownian motion and interception. Moreover, the oral cavity is the main deposition site for droplets with smaller initial diameters. Indeed, small droplets that did not deposit in the oral

cavity will evaporate completely into vapors. Deposition patterns also show gradually decreasing final droplet diameters from the pharynx to lower airways due to the continuous evaporation effect. During the expiration, evaporation continues and returned droplets become nanoscale and deposit in the oral cavity. Similarly, during the NB of pure water droplets, direct impactions of large droplets happened at the superior conchae right at the top of nares and due to the narrower passage at the nasal cavity. As a result of high filtration efficiency of the nasal cavity, only the smaller droplets were able to avoid depositing in the nasal cavity and entered the pharynx and small airways. For droplets with 10.4% NaCl, the deposition patterns show a more uniform distribution of the final droplet diameter.

The hygroscopic growth and shrinkage of droplets is a key mechanism that can influence the droplet trajectory and deposition locations (Feng et al., 2016). To investigate such effects on deposition patterns, the regional and total droplet deposition fractions (DF) (Haghnegahdar et al., 2018) are provided in Fig. 10 for 6 different exposure conditions (also see Section 2 for details). NB cases show higher DF in the nasal cavity compared with the MB cases, indicating the better filtration efficiency of the nasal cavity than the oral cavity. Furthermore, the better filtration performance of nose prohibits IAV-droplet entering the pharynx, which can be demonstrated by the lower DF in pharynx for the MB cases. In addition, the total DFs of NB cases are slightly higher than MB cases due to an increased deposition of small droplets when they pass the narrow nasal passages. DF comparisons for droplets with compositions show an increase in the total deposition with the increase in NaCl concentration. Due to the higher initial NaCl concentration in droplets, higher water vapor absorption and higher droplet growth are expected. Hence, the deposition increases accordingly in the upper airways. However, DFs at the primary regions of contact, i.e., the oral cavity for MB and nasal cavity for NB, was higher for pure water droplets than the other two types of droplets with NaCl. Specifically, the quantitative data of regional and total DF comparisons show that for MB cases, with a 53% increase in the NaCl content (from 6.8% to 10.4% NaCl), the total deposition increases by 6.72%. The pharynx DF increases by 8.85% and the oral cavity DF increases by 2.22%. However, comparisons between the 6.8% NaCl containing droplets and pure water droplets show that the increase in NaCl composition leads to an increase of the total DF by 2.2% and the increase of the pharyngeal DF by 26.54%. Also, it results in a 10.6% decrease of the regional DF in the oral cavity. Similarly for NB cases, with a 53% increase in the NaCl content (from 6.8% to 10.4% NaCl), the total deposition increases by 6.89%. The pharynx DF increases by 14.3% and the nasal cavity DF increases by 5.22%. However, comparisons between the 6.8% NaCl containing droplets and pure water droplets show that the increase in NaCl composition leads to an increase of the total DF by 1.4% and the increase of the pharyngeal DF by 39.74%. Also, it results in a 5.95% decrease in the nasal cavity DF. In addition, Fig. 10 shows that the mean diameters of the deposited droplets in the MB cases are lower than NB cases. There are two possible reasons: (1) The nasal cavity can trap large droplets more efficiently than the oral cavity; and (2) the relatively lower RH in upper airways of MB cases restrict the condensation rate while enhancing the evaporation rate. In contrast, due to the smaller size of the droplets, the number of escaped droplets to the distal sections of the lung was higher for mouth breathers. As a result, more IAV-laden droplets are able to enter and infect lower airways for the MB cases.

6.4. After-deposition dynamics of IAV-laden droplets

Compared with previous studies without accurate IAV lung uptake predictions, the multiscale CFPD-HCD model in this study provides the unique modeling capability to predict immune system responses after IAV infection with realistic breathing conditions and the resultant lung deposition data. Specifically, the local within-host cell dynamics and the virus replication help to determine the local infection sites and the immune system responses in the respiratory system. The droplet deposition data shows the population of active virus agents in the human respiratory system. Exposure to a sneezing event with a distance of 3 feet prompted an acute infection for IAV (Knight, 1980). Fig. 11 shows the host cells ($\underline{T}_T$ and $\underline{R}$) dynamics and 50% human infectious dose [HID_{50}] in the unit of $TCID_{50}$ per secretion volume, as well as the resultant IFN ($\underline{F}$). A timespan of 12 dpi was simulated using the CFPD-HCD model, during the NB at the nasal cavity (NC) and pharynx (PY), and during the MB at the oral cavity (OC) and pharynx (PY). The local threshold of clinical symptoms was determined when 10% of the epithelial cells are desquamated (Bocharov & Romanyukha, 1994) until $\underline{I}$ has reached 5% of its lowest population.

For the NB case, the highest DFs are in NC and PY are independent of the droplet composition. The numbers of virus-laden droplets deposited in the NC are close between droplets with $Y_{NaCl} = 0$ and $Y_{NaCl} = 0.104$. For the deposition in the PY, droplets with $Y_{NaCl} = 0.104$ deposit 38% higher more than droplets with $Y_{NaCl} = 0$. As a result of higher DFs, higher viral loads are expected to be available to the local epithelium, but is negligible when the deposited IAV masses were converted into $TCID_{50}$. The local HCDs in NC and PY show that the high DF and epithelial cells in NC lead to more than 2 times the conversion of susceptible cells to refractory state (Fig. 11 (a)). More IFNs were released in NC with 1.14 times higher amount with longer duration (0.35 days) compared to the number in PY (Fig. 11 (c)). However, the $\underline{T}_T$ profiles present similar minimum values between PY and NC, which is because that the higher surface area at the NC provides more immune system agents. Thus, the infection was prevented from causing severe damage to the tissue layers (Fig. 11 (b)). Also, the virus titer shows comparable infection severity at PY and NC during NB. As IIS and AIS were being removed the virus progenies, the cells were shifting back to the susceptible state, and the total apoptosis of epithelium at 12 dpi are 76.4% and 78.7% of the initial cell populations at NC and PY (see Fig. 11 (a)). The regional respiratory symptom threshold was determined at 0.91 to 5.24 dpi in NC, and 0.85 to 5.26 dpi in PY. The systemic symptom was predicted to be initiated with a 1-day delay from the respiratory symptom threshhold based on symptom score data provided by Knight (1980); Carrat et al. (2008). As a result, the systemic symptom threshold in NC is between 1.91 to 6.24 dpi, and 1.85 to 6.26 dpi in PY during NB. The duration of symptom in the PY is longer than in the NC, since the AIS and IIS are more available in NC.

Once the IAVs are inhaled *via* MB, the highest DFs can be found in OC and PY. Similar to NB cases, the droplet composition does not impose a significant alteration on the local viral load. The comparison of local HCD in the OC and PY show a higher epithelial cell

population in the PY but similar DFs. The maximum population of the refractory cell is 1.87 times higher and IFN cytokine release is 2.01 times more in the PY compared to in the OC (see Fig. 11 (d) and (e)). The duration of IFN release was similar due to the similarity between the surface area at PY and OC. The same $\underline{T}_T$ minimum value between PY and NC are due to the similarity on the viral load and the responses from immune systems agents (Fig. 11 (d)). The virus titer showed a similar trend but slightly higher peak infection titer in the PY compared within the OC due to the 15.3% higher DF of IAV-laden droplets with $Y_{NaCl} = 0.104$ in the PY, leading to the elevated infection in PY and OC. By increasing the IIS and AIS agents populations, the refractory cells shifted back to the susceptible state, and the total apoptosis of epithelium at 12 dpi was predicted as 74.7% in PY and 68.6% in the OC of the initial cell population (see Fig. 11 (d)). The local respiratory symptom threshold is at 0.62 to 5.44 dpi in OC and 0.66 to 5.56 dpi in PY. The threshold of the systemic symptom is from 1.62 to 6.44 dpi in OC and from 1.66 to 6.26 dpi in PY during NB.

Inhalations of IAV-laden droplets *via* MB and NB lead to different depositions, infections, and immune system responses. In this study, the mucus clearance in OC and NC were neglected. In all cases, the virus titer decreases below the value at 5.6 dpi which represents an increased level of relief from flu symptoms (see Fig. 11 (b) and (e)). Comparatively, infections in PY induced by the inhaled IAV-laden droplets *via* NB and MB show higher virus titers. The clinical symptoms reflected in the simulation results occuring in the OC are faster than NC due to the less amount of available immune system agents. It also indicates a more extended recovery period. As demonstrated by this *in-silico* study, the major low strain (H1N1 and H3N2) IAV replication activities happened in the upper airway tissues. Therefore, higher accumulation of activated dendritic cells as representative of AIS activation can be identified in PY regions.

7. Conclusions

A multiscale CFPD-HCD model is developed and the *in-silico* epidemiological study is presented to investigate the transport, deposition, and resultant immune system responses of the low-strain IAV laden droplets in a subject-specific human respiratory system. Both mouth and nasal breathing patterns were studied. The hygroscopic growth and shrinkage behaviors of droplets with different water-NaCl compositions were simulated and compared. The CFPD-HCD model shows the capability of predicting the local virus replication and population variations of the relative tissue agents. According to the parametric analyses in this study, the quantitative conclusions are listed as follows:

- The CFPD-HCD modeling results demonstrate that low-strain (H1N1 and H3N2) IAV replication occurs in the upper airway tissues which agree with existing experimental discovery.
- For the mouth breathing (MB) case, the droplet deposition fraction in the oral cavity was 26.4%, 23.7%, and 24.1% for droplets with NaCl mass fraction of 0, 0.068, and 0.104, respectively. No monotonic trend of the regional deposition was identified with the increase of NaCl mass fraction in droplets.
- For the nasal breathing (NB) case, the droplet deposition fraction in the nasal cavity was 48.1%, 45.2%, and 47.6% for droplets with NaCl mass fraction of 0, 0.068, and 0.104, respectively. No monotonic trend of the regional deposition was identified either with the increase of NaCl mass fraction in droplets.
- Due to the high filtration efficiency on large particles of the nasal cavity compared with the oral cavity, only smaller droplets are able to avoid being trapped in the nasal cavity and penetrate to the pharynx and distal sections. Specifically, the pharynx deposition fraction was significantly lower in MB cases than NB cases.
- For the mouth breathing (MB) cases, the average diameter of deposited droplets is less than the nasal breathing (NB) cases.
- As the representative of adaptive immune system activation, higher accumulation of activated dendritic cells was identified in the pharynx and oral cavity for the mouth breathing (MB) cases and similarly in the pharynx and nasal cavity for the nasal breathing (NB) cases.
- In the absence of mucus clearance, the average onset of systemic symptom was estimated at 1.88 dpi for NB and 1.64 dpi for MB. It indicates the faster infection distribution and immune system response for the MB cases because of the less efficient filtration effect in the oral cavity than the nasal cavity in the NB cases.

8. Limitations and future work

The biological system can be affected by a vast number of factors that makes the numerical simulation highly complex and challenging (Dobrovolny, Reddy, Kamal, Rayner, & Beauchemin, 2013). Hence, an advanced *in-silico* 3D cell culture media model is needed to consider the inter-cellular communication in the realistic physiology of the tissue. More *in vitro* and *in vivo* data regarding the host cell and immune system responses are also necessary for the model optimization using machine learning approaches in the future. To develop a more advanced CFPD-HCD model, future research tasks include:

- Considering the subject-specific human airway configurations for with pre-existing lung diseases, e.g., emphysema and COPD.
- Employing the glottal adduction and abduction motion, which may significantly influence the transport and deposition of IAV-laden droplets and the resultant local IAV deposition and replication.
- Including the movement of the periciliary fluid layer by modeling cilia propulsions and in tissue spatial distribution of the cell population, e.g., T cell movement within lymph nodes, *via* employing the agent-based model.
- Modeling the resuspension of IAV from the periciliary fluid layer and investigating the enhancement of the transport of the viral agent to small airways. The same framework can be employed for the evaluation of HID_{50} in the human exhalation at different

times post-infection.

Acknowledgments

This work was supported by the National Institute of General Medical Sciences of the National Institute of Health under Award Number P20GM103648. The use of ANSYS software (Canonsburg, PA, USA) as part of the ANSYS-CBBL academic partnership agreement is gratefully acknowledged (Dr. Thierry Marchal, Global Industry Director).

Appendix A. Supplementary data

Supplementary data to this article can be found online at https://doi.org/10.1016/j.jaerosci.2019.04.009.

References

Baccam, P., Beauchemin, C., Macken, C. A., Hayden, F. G., & Perelson, A. S. (2006). Kinetics of influenza a virus infection in humans. *Journal of Virology, 80*, 7590–7599.
Beauchemin, C. A., & Handel, A. (2011). A review of mathematical models of influenza a infections within a host or cell culture: Lessons learned and challenges ahead. *BMC Public Health, 11*, S7.
Bocharov, G., & Romanyukha, A. (1994). Mathematical model of antiviral immune response iii. influenza a virus infection. *Journal of Theoretical Biology, 167*, 323–360.
Boianelli, A., Nguyen, V. K., Ebensen, T., Schulze, K., Wilk, E., Sharma, N., et al. (2015). Modeling influenza virus infection: A roadmap for influenza research. *Viruses, 7*, 5274–5304.
Canini, L., & Carrat, F. (2011). Population modeling of influenza a/h1n1 virus kinetics and symptom dynamics. *Journal of Virology, 85*, 2764–2770.
Carrat, F., Vergu, E., Ferguson, N. M., Lemaitre, M., Cauchemez, S., Leach, S., et al. (2008). Time lines of infection and disease in human influenza: A review of volunteer challenge studies. *American Journal of Epidemiology, 167*, 775–785.
Daly, B. J., & Harlow, F. H. (1970). Transport equations in turbulence. *The Physics of Fluids, 13*, 2634–2649.
Darquenne, C. (2012). Aerosol deposition in health and disease. *Journal of Aerosol Medicine and Pulmonary Drug Delivery, 25*, 140–147.
De Andrea, M., Ravera, R., Gioia, D., Gariglio, M., & Landolfo, S. (2002). The interferon system: An overview. *European Journal of Paediatric Neurology, 6*, A41–A46.
Dobrovolny, H. M., Reddy, M. B., Kamal, M. A., Rayner, C. R., & Beauchemin, C. A. (2013). Assessing mathematical models of influenza infections using features of the immune response. *PLoS One, 8*, e57088.
Duguid, J. (1946). The size and the duration of air-carriage of respiratory droplets and droplet-nuclei. *Epidemiology and Infection, 44*, 471–479.
Eames, I., Tang, J., Li, Y., & Wilson, P. (2009). *Airborne transmission of disease in hospitals*.
Edgar, T. F., Himmelblau, D. M., & Lasdon, L. S. (2001). *Optimization of chemical processes.* McGraw-Hill.
Effros, R. M., Hoagland, K. W., Bosbous, M., Castillo, D., Foss, B., Dunning, M., et al. (2002). Dilution of respiratory solutes in exhaled condensates. *American Journal of Respiratory and Critical Care Medicine, 165*, 663–669.
El Golli, S., Arnaud, G., Bricard, J., & Treiner, C. (1977). Evaporation of volatile solvent from saline multi-component droplets carried in a stream of air. *Journal of Aerosol Science, 8*, 39–54.
Farmer, S. (1991). *The airway epithelium: Physiology, pathophysiology, and pharmacology*, *Vol. 55*. Marcel Dekker.
Feng, Y., & Kleinstreuer, C. (2013). Analysis of non-spherical particle transport in complex internal shear flows. *Physics of Fluids, 25* 091904.
Feng, Y., Kleinstreuer, C., Castro, N., & Rostami, A. (2016). Computational transport, phase change and deposition analysis of inhaled multicomponent droplet–vapor mixtures in an idealized human upper lung model. *Journal of Aerosol Science, 96*, 96–123.
Feng, Y., Zhao, J., Kleinstreuer, C., Wang, Q., Wang, J., Wu, D. H., & Lin, J. (2018). An in silico inter-subject variability study of extra-thoracic morphology effects on inhaled particle transport and deposition. *Journal of Aerosol Science, 123*, 185–207.
Ferron, G. (1977). The size of soluble aerosol particles as a function of the humidity of the air. application to the human respiratory tract. *Journal of Aerosol Science, 8*, 251–267.
Fritz, R. S., Hayden, F. G., Calfee, D. P., Cass, L. M., Peng, A. W., Alvord, W. G., et al. (1999). Nasal cytokine and chemokine responses in experimental influenza a virus infection: Results of a placebo-controlled trial of intravenous zanamivir treatment. *The Journal of Infectious Diseases, 180*, 586–593.
Guilmette, R. A., Wicks, J. D., & Wolff, R. K. (1989). Morphometry of human nasal airways in vivo using magnetic resonance imaging. *Journal of Aerosol Medicine, 2*, 365–377.
Haghnegahdar, A., Feng, Y., Chen, X., & Lin, J. (2018). Computational analysis of deposition and translocation of inhaled nicotine and acrolein in the human body with e-cigarette puffing topographies. *Aerosol Science and Technology, 52*, 483–493.
Hamborsky, J., Kroger, A., Wolfe, S., for Disease Control, C., Prevention, et al. (2015). *Epidemiology and prevention of vaccine-preventable diseases.* US Department of Health & Human Services, Centers for Disease Control and Prevention.
Handel, A., Longini, I. M., Jr., & Antia, R. (2007). Neuraminidase inhibitor resistance in influenza: Assessing the danger of its generation and spread. *PLoS Computational Biology, 3* e240.
Han, Z., Weng, W., & Huang, Q. (2013). Characterizations of particle size distribution of the droplets exhaled by sneeze. *Journal of The Royal Society Interface, 10*, 20130560.
Hayden, F. G., Fritz, R., Lobo, M. C., Alvord, W., Strober, W., & Straus, S. E. (1998). Local and systemic cytokine responses during experimental human influenza a virus infection. relation to symptom formation and host defense. *Journal of Clinical Investigation, 101*, 643–649.
Hayden, F. G., Treanor, J. J., Betts, R. F., Lobo, M., Esinhart, J. D., Hussey, E. K., et al. (1996). Safety and efficacy of the neuraminidase inhibitor gg167 in experimental human influenza. *Journal of the American Medical Association, 275*, 295–299.
Hinds, W. C. (2012). *Aerosol technology: Properties, behavior, and measurement of airborne particles.* John Wiley & Sons.
Holder, B. P., & Beauchemin, C. A. (2011). Exploring the effect of biological delays in kinetic models of influenza within a host or cell culture. *BMC Public Health, 11*, S10.
Knight, V. (1980). Viruses as agents of airborne contagion. *Annals of the New York Academy of Sciences, 353*, 147–156.
Kreidenweis, S., Koehler, K., DeMott, P., Prenni, A., Carrico, C., & Ervens, B. (2005). Water activity and activation diameters from hygroscopicity data-part i: Theory and application to inorganic salts. *Atmospheric Chemistry and Physics, 5*, 1357–1370.
Lambert, A. R., O'shaughnessy, P. T., Tawhai, M. H., Hoffman, E. A., & Lin, C.-L. (2011). Regional deposition of particles in an image-based airway model: Large-eddy simulation and left-right lung ventilation asymmetry. *Aerosol Science and Technology, 45*, 11–25.
Langtry, R. B., & Menter, F. R. (2009). Correlation-based transition modeling for unstructured parallelized computational fluid dynamics codes. *AIAA Journal, 47*, 2894–2906.
Larson, E. W., Dominik, J. W., Rowberg, A. H., & Higbee, G. A. (1976). Influenza virus population dynamics in the respiratory tract of experimentally infected mice. *Infection and Immunity, 13*, 438–447.
Lee, H. Y., Topham, D. J., Park, S. Y., Hollenbaugh, J., Treanor, J., Mosmann, T. R., et al. (2009). Simulation and prediction of the adaptive immune response to influenza a virus infection. *Journal of Virology, 83*, 7151–7165.
Li, W., Montassier, N., & Hopke, P. (1992). A system to measure the hygroscopicity of aerosol particles. *Aerosol Science and Technology, 17*, 25–35.

Liu, L., Li, Y., Nielsen, P. V., Wei, J., & Jensen, R. L. (2017). Short-range airborne transmission of expiratory droplets between two people. *Indoor Air, 27*, 452–462.
Male, D., Brostoff, J., Roth, D., & Roitt, I. (2006). *Immunology* (7th ed.). Elsevier.
Ma, B., & Lutchen, K. R. (2009). Cfd simulation of aerosol deposition in an anatomically based human large–medium airway model. *Annals of Biomedical Engineering, 37*, 271.
Menter, F. R. (1994). Two-equation eddy-viscosity turbulence models for engineering applications. *AIAA Journal, 32*, 1598–1605.
Mikhailov, E., Vlasenko, S., Niessner, R., & Pöschl, U. (2004). Interaction of aerosol particles composed of protein and salts with water vapor: Hygroscopic growth and microstructural rearrangement. *Atmospheric Chemistry and Physics, 4*, 323–350.
Miller, R., Harstad, K., & Bellan, J. (1998). Evaluation of equilibrium and non-equilibrium evaporation models for many-droplet gas-liquid flow simulations. *International Journal of Multiphase Flow, 24*, 1025–1055.
Miller, J., & Mitchell, G. (1969). Thymus and antigen-reactive cells. *Immunological Reviews, 1*, 3–42.
Nowak, M., & May, R. M. (2000). *Virus dynamics: Mathematical principles of immunology and virology: Mathematical principles of immunology and virology*. UK: Oxford University Press.
Oguin, T. H., Sharma, S., Stuart, A. D., Duan, S., Scott, S. A., Jones, C. K., et al. (2014). Phospholipase d facilitates efficient entry of influenza virus, allowing escape from innate immune inhibition. *Journal of Biological Chemistry, 289*, 25405–25417.
Ou, C., Li, Y., Wei, J., Yen, H.-L., & Deng, Q. (2017). Numerical modeling of particle deposition in ferret airways: A comparison with humans. *Aerosol Science and Technology, 51*, 477–487.
Pawelek, K. A., Huynh, G. T., Quinlivan, M., Cullinane, A., Rong, L., & Perelson, A. S. (2012). Modeling within-host dynamics of influenza virus infection including immune responses. *PLoS Computational Biology, 8*, e1002588.
Petrie, S. M., Guarnaccia, T., Laurie, K. L., Hurt, A. C., McVernon, J., & McCaw, J. M. (2013). Reducing uncertainty in within-host parameter estimates of influenza infection by measuring both infectious and total viral load. *PLoS One, 8*, e64098.
Pinilla, L. T., Holder, B. P., Abed, Y., Boivin, G., & Beauchemin, C. A. (2012). The h275y neuraminidase mutation of the pandemic a/h1n1 influenza virus lengthens the eclipse phase and reduces viral output of infected cells, potentially compromising fitness in ferrets. *Journal of Virology, 86*, 10651–10660.
Rennie, C. E., Gouder, K. A., Taylor, D. J., Tolley, N. S., Schroter, R. C., & Doorly, D. J. (2011). Nasal inspiratory flow: At rest and sniffing. *International forum of allergy & rhinology: Vol. 1*, (pp. 128–135). Wiley Online Library.
Schaffer, F., Soergel, M., & Straube, D. (1976). Survival of airborne influenza virus: Effects of propagating host, relative humidity, and composition of spray fluids. *Archives of Virology, 51*, 263–273.
Scharfman, B., Techet, A., Bush, J., & Bourouiba, L. (2016). Visualization of sneeze ejecta: Steps of fluid fragmentation leading to respiratory droplets. *Experiments in Fluids, 57*, 24.
Scheinherr, A., Bailly, L., Boiron, O., Lagier, A., Legou, T., Pichelin, M., et al. (2015). Realistic glottal motion and airflow rate during human breathing. *Medical Engineering & Physics, 37*, 829–839.
Schroeter, J. D., Asgharian, B., Price, O. T., Kimbell, J. S., Kromidas, L., & Singal, M. (2016). Simulation of the phase change and deposition of inhaled semi-volatile liquid droplets in the nasal passages of rats and humans. *Journal of Aerosol Science, 95*, 15–29.
Simion, A. I., Grigoraş, C. G., Roşu, A. M., & Gavrilă, L. (2015). Mathematical modelling of density and viscosity of nacl aqueous solutions. *Journal of Agroalimentary Processes and Technologies, 21*, 41–52.
Smith, A. M., & Perelson, A. S. (2011). Influenza a virus infection kinetics: Quantitative data and models. *Wiley Interdisciplinary Reviews: Systems Biology and Medicine, 3*, 429–445.
Tellier, R. (2009). Aerosol transmission of influenza a virus: A review of new studies. *Journal of the Royal Society Interface* rsif20090302.
Treybal, R. E. (1980). *Mass transfer operations*, *466* New York.
Wang, Y., James, P., et al. (1999). On the effect of anisotropy on the turbulent dispersion and deposition of small particles. *International Journal of Multiphase Flow, 25*, 551–558.
Ward, C., Dempsey, M., Ring, C., Kempson, R., Zhang, L., Gor, D., et al. (2004). Design and performance testing of quantitative real time pcr assays for influenza a and b viral load measurement. *Journal of Clinical Virology, 29*, 179–188.
Weise, T. (2009). *Global optimization algorithms-theory and application.* Self-published.
Weissenborn, P. K., & Pugh, R. J. (1996). Surface tension of aqueous solutions of electrolytes: relationship with ion hydration, oxygen solubility, and bubble coalescence. *Journal of Colloid and Interface Science, 184*(2), 550–563.
Whitaker, S. (1972). Forced convection heat transfer correlations for flow in pipes, past flat plates, single cylinders, single spheres, and for flow in packed beds and tube bundles. *AIChE Journal, 18*, 361–371.
Wilcox, D. C., et al. (1998). *Turbulence modeling for CFD*, *Vol. 2.* CA: DCW industries La Canada.
Worth Longest, P., & Xi, J. (2008). Condensational growth may contribute to the enhanced deposition of cigarette smoke particles in the upper respiratory tract. *Aerosol Science and Technology, 42*, 579–602.
Yang, W., Elankumaran, S., & Marr, L. C. (2011). Concentrations and size distributions of airborne influenza a viruses measured indoors at a health centre, a day-care centre and on aeroplanes. *Journal of the Royal Society Interface* rsif20100686.
Yang, W., & Marr, L. C. (2011). Dynamics of airborne influenza a viruses indoors and dependence on humidity. *PLoS One, 6*, e21481.
Zhang, Z., Kim, C. S., & Kleinstreuer, C. (2006). Water vapor transport and its effects on the deposition of hygroscopic droplets in a human upper airway model. *Aerosol Science and Technology, 40*, 1–16.
Zhang, Z., Kleinstreuer, C., & Feng, Y. (2012a). Vapor deposition during cigarette smoke inhalation in a subject-specific human airway model. *Journal of Aerosol Science, 53*, 40–60.
Zhang, Z., Kleinstreuer, C., & Hyun, S. (2012b). Size-change and deposition of conventional and composite cigarette smoke particles during inhalation in a subject-specific airway model. *Journal of Aerosol Science, 46*, 34–52.